2013

Characterisation of bulk silicon diodes for the magic plate 512 dosimeter array

Daniel Robinson
University of Wollongong

Characterisation of Bulk Silicon Diodes for the Magic Plate 512 Dosimeter Array

A thesis submitted in fulfilment of the
requirements for the award of the degree

Master of Science Research

from

UNIVERSITY OF WOLLONGONG

by

Daniel Robinson
Bachelor of Medical Radiation Physics
University of Wollongong, 2011

FACULTY OF ENGINEERING AND INFORMATION SCIENCES,
CENTRE FOR MEDICAL RADIATION PHYSICS
2013

Abstract

The aim of this study is the characterisation of an innovative silicon 2D array Detector named Magic Plate 512 for dosimetry in four-dimensional small field external beam radiotherapy. The need for such a device arises from the inability of current commercial dosimetric devices to account for thoracic movement during 4-dimensional radiation therapy (4DRT). 4DRT represents the next step from intensity modulated radiation therapy (IMRT), where organ movements during treatment are no longer neglected as the treatment beam will actively follow a target volume. Dynamic multi-leaf collimators (DMLCs) are one solution to this issue of patient respiration as a DMLC will continuously reshape the treatment aperture to compensate for target motion [1].

The Magic Plate 512 (M512) is a 2D dosimeter array utilizing 512 silicon detectors on a bulk p-type substrate, which has been designed as a high resolution quality assurance tool to determine penumbral variations as a result of simulated patient respiration by a phantom. This variation will be compared with the 4DRT software to determine the accuracy and effectiveness of the DMLC treatment.

Test structure diodes have been fabricated on two sets of silicon substrates: one from an American silicon wafer provider (named CMRP) with resistivity of 10 cm and 1 cm, the second set from an European silicon facility (named KDB) with resistivity of 10 cm, diodes were fabricated from both substrates with, and without an n+ guard ring. Electrical characterisation as well as radiation damage studies from both photons and photoneutrons were undertaken on these test structures.

The purpose of these tests was to determine the optimal configuration regarding ion implantation, substrate type and resistivity as well as determining the effect of a guard ring on the charge collection efficiency and dose response. Increased concentrations of ion implantations were found to decrease both leakage current and device capacitance as well as showing a smaller response decrease as a result of both photon and neutron damage. The CMRP substrate demonstrated a smaller response decrease than the KDB substrate, whilst it was found the guard ring had little to no effect on either leakage current or capacitance.

Two Magic Plate 512 arrays were constructed as a result of these test structure characterisations and subjected to electrical characterisations and radiation damage studies. The two magic plate arrays utilized a 10 cm(CMRP) substrate and 100 μC ion implantation (array #10) and another with the 10 cm(KDB) substrate and 30 μC ion implantation (array #24). The electrical characterisation of these two devices found the leakage current was considerably higher for array #24, whilst a comparison of diode position to leakage current found that the position of the diode in the array has no effect on the magnitude of leakage current. The radiation damage tests found results consistent with those of the test structures, although the absolute response of the diodes fabricated on the CMRP substrate was so low that the calculated uncertainties are too large to make any conclusions from the data. As such it was determined that array #24 with the diodes fabricated on the KDB substrate provides a more stable response to radiation damage and presents as the more viable option for small field radiation dosimetry.

Materials and findings in this research project were included partially to a paper submitted to IEEE TNS Characterisation of an innovative p-type epitaxial diode for dosimetry in modern external beam radiotherapy A.H. Aldosari, A. Espinoza, D. Robinson, I. Fuduli, C. Porumb, S. Alshaikh, M. Carolan, M.L.F. Lerch, V. Perevertaylo, A.B. Rosenfeld, Member, IEEE, M. Petasecca, Member, IEEE. Data relative to MP512 will be used for a publication in Medical Physics which is currently in preparation.

Statement of Originality

This is to certify that the work described in this thesis is entirely my own, except where due reference is made in the text.

No work in this thesis has been submitted for a degree to any other university or institution.

Signed

Daniel John Robinson
24^{th} of November, 2013

Acknowledgments

I would firstly like to my principal supervisor Dr. Marco Petasecca for all the time and effort he has put towards this project, and my co-supervisor Prof. Anatoly Rosenfeld for designing the detectors used in this study. Secondly, I would like to thank Dr. Martin Carolan, Chief Physicist of the Illawarra Cancer Care Centre for his supervising role in the many diode response tests.

I would like to extend my gratitude towards Mr Anthony Espinoza, Anthony's assistance as well as his infinite patience helped greatly in the completion of this project and I cannot thank him enough.

I would also like to extend my gratitude to the following people, all of whom contributed to this project:

- Dr. Dean Cutajar
- Dr. Mitra Safavi
- Dr. Michael Lerch
- Abdullah Aldosari
- Ziyad Alrowaili
- Dane Pope
- Claudiu Poroumb
- Michael Weaver

- Karen Ford
- Peter Ihnat

Finally a special thank you to my Mum, Dad and my sister for supporting me and putting up with me throughout the course of my studies, your support was invaluable and I couldn't have done this without you.

Contents

List of Figures

List of Tables

Chapter 1

Literature Review

1.1 Radiation Therapy

Radiation therapy is the use of ionizing radiation for the purpose of treating malignant cells, often used in conjunction with chemotherapy and surgery. Radiation can be delivered either by an external MeV x-ray beam or via implanted radioisotopes. The total dose per treatment is dependent on tumour size and location and frequency of delivery, though typically between 20-80 Gy. Regardless of the delivery method, the aim of the irradiations is to damage the DNA structures of the cancerous tissue via the process of double strand breaks, and disrupt or halt its reproductive cycle. Double strand breaks refer to the process whereby incident particles sever both strands in the DNA's double helix. A radiation dose is prescribed depending upon the location and type of cancerous tissue, then delivered to the patient with the goal of delivering the specified dose to the target area. This prescription, whilst aiming to deliver maximum dose to the target area, must keep dose to surrounding normal structures low enough so as to prevent any side effects [2].

External beam radiation therapy can be classified in terms of the energy of the beam utilized,

- Orthovoltage/Superficial x-rays: These utilize an energy range of ≈50-300

keV, and as such, the lower photon energies increase the photoelectric cross section and the probability of photoelectric effect interaction is greater, decreasing the penetrability of the beam. This decreased penetration depth in comparison to megavoltage x-rays leads to an orthovoltage x-ray beam only being useful for small superficial tumours such as skin cancers.

- Megavoltage x-rays: Utilize an energy range of 4-18 MeV and due to this increased energy range in comparison to orthovoltage x-rays, are used for tumours located deeper within the body at depths inaccessible for orthovoltage x-rays to reach.

1.1.1 Intensity Modulated Radiation Therapy

Intensity modulated radiation therapy (IMRT) is the evolution of the original 'step and shoot' external beam radiation therapy, which utilized a fixed beam cross section rather than a dynamic cross section as in IMRT. IMRT treatment plans attempt to minimize dose to surrounding healthy tissue by creating target volumes, which emulate the shape of the tumour itself. This target is defined by combining CT (computed tomography) images with 3D computer modeling. CT is an imaging modality which uses digital processing of x-ray images to create a 3D image of a target area. The process is achieved via multiple beam delivery angles along with multi-leaf collimators (MLC's). Both the multiple beam angles and MLC's allow for reduced dose to surrounding healthy tissue. The MLC's consist of a large number of metal leaves, generally made of Tungsten, which move independently to modulate the beam. This beam modulation allows for better conformity of dose delivered to the target volume, whilst minimizing the dose to any surrounding tissues or structures.

Although IMRT is a far more precise delivery technique than others which preceded it, any kind of radiation therapy carries with it inherit risks due to the nature of the treatment. As such quality assurance is necessary so as to ensure positive treatment outcomes and quality of life for patients.

Volumetric modulated arc therapy (VMAT) is the next step in the evolution of IMRT. It is a treatment modality which utilizes one or more beam arcs with continuously varying beam aperture, rotational speed of the gantry head and dose rate [3]. This continuous approach utilizes the advancements of IMRT in the range of beam orientations but administers them in the shortest possible time.

1.1.2 4 Dimensional Radiation Therapy (4DRT)

Patient anatomy can change significantly between radiation therapy treatments, but also whilst the treatment is taking place. For lung cancers, tumour locations can move up to 2cm in the superior-inferior plane of motion, 1.5 cm in the medial-lateral plane and 1.7 cm in the anterior-posterior plane as a result of respiration [4]. This presents an issue when a patient is being treated by traditional IMRT. Interfraction motion of the treatment volume can occur as a result of rotations of the target, bowel and bladder volume changes, and weight loss as a result of treatment [5]. Intrafractional anatomic motion however consists of cardiac, digestive and respiratory motion.

As this motion is not accounted for by IMRT or conformal radiation therapy during pre treatment imaging, artifacts are created which in turn cause distortion of the target volume as well as incorrect positional and volumetric information [5]. Planning target volumes (PTV) are defined to include both interfraction and intrafraction motion, which is highly undesirable owing to the increase in exposed healthy tissue. The issue increased tissue irradiation becomes more prevalent in hypofractination treatments, with considerably higher doses than normal RT treatments, healthy tissue could be exposed to as much as 20 Gy in a single fraction.

4DRT, which is defined as ”the explicit inclusion of the temporal changes in anatomy during the imaging, planning and delivery of radiotherapy” [6], is able to account for patient respiration as well as other temporal changes in anatomy to minimise the necessary PTV by accounting for time in addition to the three spatial dimensions. This is done in conjunction with 4D CT imaging, 4D treatment planning and 4D treatment delivery.

4D CT requires the acquisition of a large number of CT images over consecutive segments of a patients breathing cycle such that the entire range of motion is imaged. 4D treatment planning creates a treatment based upon the 4DCT scans to create a unique treatment for each segment of the respiratory cycle. 4D treatment delivery involves dynamic treatment which takes into account the treatment plan for the segments of the patients breathing cycle.

Stereotactic Body Radiotherapy (SBRT) is an example of a 4DRT treatment modality. SBRT consists of the treatment of extracranial tumours by a hypofractionated treatment of one to five highly conformal high dose fractions. SBRT utilizes gold fiducials, which are implanted within the target volume prior to diagnostic imaging. Images are taken with the fiducials implanted to determine the effect of respiration or other bodily movements on target volume shape and position, to create a 4-dimensional image. The hypofractionated delivery method has proved effective with studies on early-stage peripheral non-small cell lung cancer patients showing 2-3 year local control rates greater than 90% [7].

1.2 Dosimetry

Radiation dosimetry refers to the measurement of absorbed dose in matter as a result of the interaction with ionizing radiation [8]. The focus of dosimetry in health and medical physics is the calculation of both internal and external doses for the purpose of radiation protection and quality assurance. A dosimeter is any device, which can measure the absorbed dose as a result of ionizing radiation within its own sensitive volume.

1.2.1 Absorbed Dose

Absorbed dose (D) refers to the energy imparted by ionizing matter of a particular mass in a finite volume. Attix [8] defines absorbed dose by,

$$D = \frac{d\epsilon}{dm} \tag{1.1}$$

[8] Where ϵ is the expectation value of the energy imparted in a finite volume V. dϵ is the energy imparted on an infinitesimal volume dv, with dm being a mass in dv. Absorbed dose has units of Gray (Gy), where 1 Gy is the absorption of 1 Joule per kilogram of matter.

1.2.2 Equivalent Dose

Absorbed dose is only a general term however, as it does not take into account the different types on ionizing radiation and their effect on the human body. Equivalent dose (H) however, takes this into account by introducing a radiation weighting factor (W). W is an estimated value for ionizing radiation of varying types and energies which takes into account their relative hazardousness to humans. Equivalent dose has units Sieverts (Sv) [8].

$$H_T = \sum W_R \times D_{R,T} \tag{1.2}$$

1.2.3 Fluence

Fluence refers to the integrated number of particles that intersect a unit area over a specified time period, for the purpose of dosimetry however, the mere number of particles does not provide enough information. Energy fluence (Ψ) is a field descriptive quantity which accounts for individual particles/rays as well as their respective energies. Energy fluence is expressed as Jm^{-2} or erg cm^{-2}. If R is the expectation value of all the rays/particles striking a finite volume in a defined time frame, and we reduce this finite area to an infinitesimal volume with cross sectional area da, then energy fluence (Ψ) can be defined as [8];

$$\Psi = \frac{dR}{da} \tag{1.3}$$

1.2.4 Dosimeter Properties for IMRT

Dosimeters used for IMRT should exhibit high spatial resolution and radiation hardness, as well as linearity and accuracy. These parameters are necessary to ensure they can precisely measure the external dose as well as act as a calibrating tool for the calculation of dose to a patient [9]. Dosimetric properties change due to the damaging nature of radiation, with the two fundamental damaging mechanisms being lattice displacement and ionization effects. Lattice displacement refers to particles interacting with the atoms in the crystal lattice and changing their arrangement, as a result, the number of recombination centres increases, leading to worsening analog properties. Ionization effects are caused by charged particles with energy too low to create lattice displacement, and create softer errors than those occuring as a result of lattice displacement.

Spatial resolution refers to the measurement how closely points of different dose can be resolved in a system, and is determined by the sensitive volume of a dosimeter. Smaller sensitive volumes allow for point like measurements, with small spacing and between detectors resulting in high spatial resolution. Smaller sensitive volumes also avoid the volume averaging effect observed in large ionization chambers, which is important in IMRT due to the steep dose gradients in the target volume.

Radiation hardness is a necessary property of a dosimeter to avoid their performance changing with accumulated dose. If a dosimeter is hardened however, it will be stable after an initial dose, independent of any further accumulated dose. In order to make a device radiation hardened, a number of techniques have been introduced in detector design. These include manufacturing devices on insulating substrates, shielding, choosing substrates with a wide band gap for higher tolereance to deep level effects as well as the introudcion of bi-polar integrated circuits.

When quantifying the size of dosimetric devices, commercial ionization chambers have a sensitive volume in the region of 1-10x10^{-2} cm^3 whilst commercial silicon detectors have a sensitive volume in the region of 1x10^{-1} mm^3.

1.3 Point Dosimeters

1.3.1 Ionization Chambers

Cylindrical ionization chambers are utilized for point dose measurements due to their linear response to absorbed dose, stability and traceability to a primary calibration standard [10]. Cylindrical chambers are most commonly used, as the geometry minimizes the response variation as a function of beam entry angle when the beam is perpendicular to the chamber axis due to symmetry [11]. Ionization chambers consist of a gas filled chamber with an anode and cathode, the gas is ionized by incident particles which creates an ion pair. A voltage potential applied across the chamber causes the respectively charged ions to travel to either the anode or cathode, with the accumulated charge proportional to the energy of the incident particles.

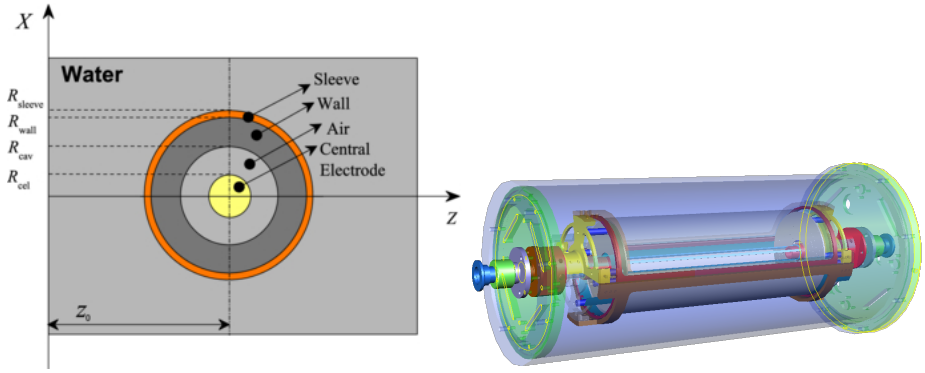

Figure 1.1 Cross section and 3D schematic of a cylindrical ionization chamber

As a result of the size of ionization chambers, volume averaging is observed. The volume averaging effect causes perturbations to the dose distribution measurements in regions with steep dose gradients, especially in the beam penumbra regions. Bouchard and Suentjens [12] provided a method for correcting chamber response to account for non uniform dose distributions. This method however was only applicable for Monte Carlo simulations, with no real world applications.

The energy response of modern ionization chambers, when considering megavoltage

photon beams is essentially flat, although this is not the case for very small chambers. In order to increase the ionization signal, a high Z material is introduced to the central anode. This does however create sensitivity variations with field size and depth. Both Wellhofer/Scanditronix CC01 and PTW PinPoint^{TM}chambers demonstrate an over response with low energy photons [13].

If an ionization chamber is functioning correctly it should demonstrate a stable response over time [10], ionization chambers can be compared against a local secondary standard ionization chamber for the purpose of quality assurance.

1.3.2 Solid State Dosimeters

Semiconductor diodes, particularly p-type silicon semiconductors, have characteristics which make them ideal for dosimetry when using megavoltage photon beams for small field measurements [10]. Solid state dosimeters operate in a manner similar to ionization chambers, although as the name suggests, incorporate a solid volume within which ionization occurs in comparison to a gas. Incident particles interact with dopants introduced into the lattice, with a potential difference imposed over the device causing ions to travel to an electrode of opposing charge. In comparison to ionization chamber detectors, semiconductor diodes generally have a much smaller active volume as well as increased sensitivity to ionizing radiation in the range of 1800 times that of an ionization chamber of the same size. Because the silicon has a relatively high atomic number compared to the gas within an ion chamber, the detector will have increased sensitivity to low energy photons, as the photoelectric effect cross section is approximately proportional to Z^5.

Due to their small size, solid state diode detectors are generally used for small field dose distribution measurements [14]. These types of detectors can also be 'energy compensated' by introducing a lead filter or shield in order to minimize their low energy sensitivity. It has been noted however that for particular p-type silicon diodes designs, they do exhibit angular dependence as much as 3% for beams perpendicular to the diode axis and as much as 15% for beams orientated near the diode axis [15].

Diamond detectors present as an alternative to silicon dosimeters in that they are close to tissue equivalent (in terms of atomic composition, although not in density). They also exhibit directional dependence smaller than that of silicon, mechanical stability, demonstrate high radiation hardness and high radiation sensitivity [16]. Bucciolini et al. [17] demonstrated that in a clinical environment, diamond detectors can actually reproduce identical results as p-type silicon for small treatment fields, although diamond detectors have in the past exhibited dose rate dependence which severely limits their use for scanning or IMRT dose distribution [17]. There has been some success removing this dose rate dependence, the Single-Crystal CVD Diamond produced by the SCIO Diamond Corporation is one such example which does not demonstrate dose rate dependence. It is however, exceedingly difficult and expensive to manufacture diamonds of sufficient quality and as such, does not present a viable option for RT dosimetry currently.

Thermoluminescence dosimeters (TLD's) are a small integrating dosimeter with near tissue equivalent composition in terms of atomic number and a density ≈ 2.6 times that of tissue. They have been commercially available since the 1970's for megavoltage x-ray dosimetry and exhibit a non-linear integrated dose response as well as energy response variations which must be evaluated before the TLD can be used [18]. They do not provide instant dose in contrast to diodes, however are very useful for in vivo dosimetry.

1.4 Two Dimensional Dosimeters

1.4.1 Radiographic Film

Radiographic film (silver halide film) has been shown to effectively determine two dimensional dose distributions in phantoms, although they do exhibit certain properties, which are undesirable for IMRT dosimetry. Film operates as a dosimetry device as incident particles interact with the film, creating a visual change where the interaction took place. This allows for the visualization of the cross sectional profile

of the beam being used. The degree of colour change of the film is proportional to the amount of ionizing radiation interacting with the film at a specific location. The nature of film does not allow for any real time dose measurements and ultimately can only detail integral dose across the specified area. Inherent flaws also arise in radiographic film as a result of the production process, leading to film batches with varying sensitivities. Radiographic film also has strong energy dependence (14-20 times) to low energy photons in comparison to high energy photons [10].

Issues have also arisen from processor conditions, densitometry artifacts and variations of the photon beam spectrum throughout the measured field [19]. According to Bogucki et al. [20] the greatest potential for creating errors when using radiographic film for dosimetry arises from the optical density variation that arise due to temperature variations in the film processor.

In spite of these obvious drawbacks, when considering the trade off between flaws, and the complexity and labour involved in using and producing film, radiographic film does present a convenient option for two dimensional dosimetry. The main reasons being the high spatial resolution and the availability of automated film processing equipment.

1.4.2 Radiochromic Film

Radiochromic film has two major benefits in comparison to radiographic film, the optical density response can be determined without the need for a processor, as well as being roughly tissue equivalent. Recent advances in film technology have superseded the Gafchromic MD-55 and HS films which up until recently have been the standard for commercial film. These films are not ideal dosimetry tools due to their relative insensitivity to ionizing radiation [21]. This sensitivity is too low to make it a practical dosimetry tool for routine IMRT measurements, Gafchromic EBT (External Beam Therapy) however was recently introduced which has an optical density similar to that of Kodak EDR (Extended Dose Range)-2 [22]. A study by Low et al. [23] demonstrated that there are three significant artefacts that can limit the ac-

curacy of Gafchromic EBT on a flatbed scanner, these being a film rotation effect which is dependent upon the orientation on a flatbed scanner, scanner uniformity and scanner bed temperature during scanning.

Pixel to pixel noise when measured at typical dose levels is greater for radiochromic film than for many other dosimetry devices such that the pixel to pixel noise may limit measurement precision for IMRT dose distribution in low dose regions as well as characterizing low dose features such as penumbra tails. Pixel averaging can be used to reduce noise but this can introduce errors in dose measurements.

1.4.3 Array Detectors

1.4.3.1 Silicon Photodiode Array

Array detectors are the evolution of individual radiation detection devices in that multiple devices are couple together to give a more detailed dose profile. In 1999 El-Mohri et al. utilized a light sensitive amorphous silicon photodiode coupled with a Si:H film transistor pixel detector for the purpose of performing relative dosimetry. The array used consisted of 512 x 512 pixels with a pitch of 508 μm over an area of 26 x 26 cm^2 [24]. Induced by radiation, charge in each pixel is integrated by a pre-amplifier and stored on a capacitor. This process is followed by a row by row readout of the array which continues until all, or a specified number of rows have been addressed. The array of photodioes were covered with a layer of scintillator CsI(Tl), producing light upon interaction with radiation, the wavelength of produced light, 550 nm, matches well to spectra sensitivity of the Si photodiode.

Characterization demonstrated a highly linear response throughout the tested signal range as well as excellent stability of response when considering both absolute and relative dosimetry. El Mohri's work was continued in 2005 with the introduction of the Active Matrix Flat Panel Dosimeter (AMFPD) for the purpose of phantom dosimetric measurements, this array was modified from the original design in order to cater for higher dose ranges. The hope was that the AMFPD would replace for in-

water equivalent phantoms, in order for this to occur the image acquisition electronics were modified so as to increase the dynamic range of the array [25].

There is a drawback to this technology, as a result of the use of a non-water equivalent high Z scintillator, CsI(Tl), which makes absolute dosimetry more difficult. The thin film transistors are also grown on a sapphire substrate which, while being photoluminescent, is angularly dependent.

1.4.3.2 Silicon Diode Array

Until 2004, Mapcheck was the only commercially available 2-D array available, it is a two-dimensional diode array utilizing n-type diodes [26]. Developed by Sun Nuclear, the Mapcheck array comprises of 445 diodes with a physical cross section of 0.8 mm^2 over a total area of 22 x 22 cm^2, the spacing of the diodes are 7.07 mm in the central 10 x 10 cm^2 region and 14.14 mm in the outer region, an effective build-up region of 2 cm and a backscattering thickness of 2.3 cm. The system shows a linear diode response up until a saturation dose of $\approx$ 2.8 Gy along with a 2% sensitivity variation when the instantaneous dose rate is varied by a factor of 3 [27]. The system is initially calibrated by the manufacturer using repeated static field irradiations, and is then rotated between irradiations in a defined sequence such that the relative calibration of each detector can be identified. The second calibration step involves calibration for absolute dosimetry, the device is irradiated to a known dose at the central axis, which allows the system to be stable for 6 months [28], the calibration does however vary with temperature by $\approx 0.5\%/\ ^{o}C$.

In 2007 Menichelli et al. designed a silicon diode array, the 6.29 x 6.29 cm^2 module comprised of 21 x 21 pixels for a total of 441 channels, of which 9 were fitted together to create a 20 x 20 cm^2 field with 3639 channels [29]. The current from each channel is integrated through a low bias op-amp and digitized, a frame clock resets the integration time by use of a voltage controlled oscillator. In order however to simplify and miniaturise the readout system, Wellhofer-Scanditronix TERA Chip designed by the INFN Turin group was introduced [30].

1.4.3.3 Ionization Chamber Arrays

Amerio et al. were the first who designed a pixel segmented ionization chamber array for the purpose of 2-D dose verification. The initial design incorporated 1020 chambers with a sensitive volume of 0.8 cm^3 over an area of 23.6 x 23.6 cm^2 with chamber diameter 4 mm, height 5.5 mm and a 7.5mm pitch [31]. The reproducibility of experiments with the array was found to be within 0.5% with stability within 1.3% over a period of 7 months as well as no dependence upon integral dose and linear dependence of signal output with dose. The original detector array developed by Amerio et al. evolved into the commercially available I'mRT MatriXX. This system is capable of measuring a dose rate ranging from 0.02-20 Gy/min with a resolution of 7.62 mm. When using linear interpolation post processing however, it is claimed to be able to be reduced down to 1mm [32].

Since the introduction of the I'mRT MatriXX PTW-Freiburg have developed two commercial ionization chamber arrays, the Version 1 and the seven29 both of which cover an area of 27 x 27 cm^2. Version 1 has 256 8 x 8 mm^2 detectors in a 16 x 16 square array whilst the seven29 has 729 5 x 5 mm^2 detectors in a 27 x 27 array. For both versions the long term reproducibility (four months) for both arrays was found to be 1% with the measured output factors showing excellent agreement to conventional chamber measurements [33].

1.4.3.4 Optimal Specifications of a 2-D Dosimeter Array for SBRT

Stereotactic body radiotherapy (SBRT) utilizes highly conformal high dose fractions which must follow accurate 4-D images to ensure positive patient outcomes. To ensure this is the case, highly accurate dosimetry is required so the patient is treated with the desired dose to the correct target volume. Any dosimetry device for SBRT requires a total sensitive area large enough to encompass the magnitude of the range of motion of any target volume (2 cm in the superior/inferior plane, 1.5 cm in the medial/lateral plane and 1.7 cm in the anterior/posterior plane for lung cancers as a result of respiration [4]). It must also contain enough channels with spatial resolution

in the order of a approximately 2 mm as well as a small active volume to ensure that the steep dose gradients can be accounted for. From the literature, at present there is no 2-D array available which has such characteristics, for this reason the CMRP has designed the MP512 array for 4DRT, specifically for stereotactic applications such as SBRT.

1.4.4 Photoneutrons

Modern medical linear accelerators are capable of delivery x-ray or electron beam energies up to and including 25 MeV. Traditionally, beam energies of this magnitude were not necessary, due to the increase in overweight and obese patients however, increased beam energies are required to the greater penetration requirements of the beam. This increased energy however can lead to the introduction of photoneutrons, creating a mixed radiation field. These photoneutrons occur as a result of the energy of incident photons being greater than the nuclear binding energy of that material with which the photons are interacting. A process known as giant dipole resonance occurs whereby the material either emits a neutron as a result of high frequency collection excitation of atomic nuclei.

Photons with energies greater than 7 MeV can generate neutrons through interactions with the various structures throughout the accelerator. These interactions are more prominent in high Z materials such as the target and primary collimators [34]. These photons can penetrate the linac as well as deposit dose within a patient themselves. At these increased energies, photoneutrons in conjunction with greater photon leakage can be responsible for a greater probability of fatal secondary malignancies. A recent study by Kry et al. [35] found that the risk of a fatal secondary malignancy as a result of an IMRT prostate treatment increased from 2.1% for a 10 MeV beam to 5.1% for an 18 MeV beam.

A recent study by Howell et al. [36] investigated the secondary neutron spectrums from Varian, Siemens and Elekta linacs, all of which utilized MLC technology. One of the conclusions that they found from their results was that the total number of sec-

ondary neutrons is dependent upon the initial photon spectra, the greater the number of photons with energies above the (γ,n) threshold (nuclear binding energy of the incident material), the greater the number of reactions and as a result a greater the number of secondary neutrons than a beam with energies below the (γ,n) threshold. Using a 10 x 10 cm^2 field at a SSD of 100 cm they determined for a 15MeV beam, closed jaws and MLC contributed to a neutron dose of 7.4x10^{-3} μSv/MU, 1.7x10^{-3} μSv/MU and 3.1x10^{-3} μSv/MU for the Varian 21EX, Elekta Precise and Siemens ONCOR respectively [36]. When the beam energy was increased to 18 MeV as expected the equivalent dose per MU increased to 1.3x10^{-2} μSv/MU, 5.5^{-3} μSv/MU and 3.8^{-3} μSv/MU for respectively.

The liberated photoneutrons have the potential to create problems in treating patients through neutron capture by either nitrogen or hydrogen. Neutron capture occurs when a liberatd neutron is absrobed into the atomic nucleus, as a result both a photon and electron are ejected from the atom. Thermal neutrons which interact with nitrogen release a 0.58 MeV proton which has a range of $\approx$10 μm in tissue whilst those interacting with hydrogen release a 2.2 MeV γ-ray photon. The hydrogen capture is the dominant process which contributes to the greater dose for both thermal and intermediate neutrons as intermediate neutrons will become thermalized within the body [8]. A study by Kry et al. [35] found that for photoneutrons created during an 18 MeV photon irradiation, neutron fluence peaked at $\approx$2 cm within a patient equivalent phantom. An inverse square fluence decrease occurred as the depth increased.

1.5 Radiation Damage in Silicon

Radiation damage in silicon detectors can be divided into categories of surface and bulk damage. It is primarily bulk damage, which is the limiting factor when considering the use of silicon detectors in intense radiation fields [37]. Surface damage leads to an increase of leakage current, but this can be minimised by the use of silicon detectors in passive mode with no applied bias. Bulk damage in silicon is primarily

caused by highly energetic leptons, as well as hadrons, displacing a *primary knock on atom* (PKA) out of its lattice. This results in a silicon interstitial and a left over vacancy known as a Frenkel pair. These both are able to migrate through the lattice and form point defects with impure dopants within the silicon structure. The displacement of the primary recoil atom however, can only occur if the energy imparted is greater than the threshold energy ($\approx$ 25 eV). Energy loss along these recoil paths occur as a result of both ionization and further displacements. Non-ionizing defects become prevalent at the end of any heavy recoil and create a dense agglomeration of defects seen in Fig 1.2, known as clusters [37].

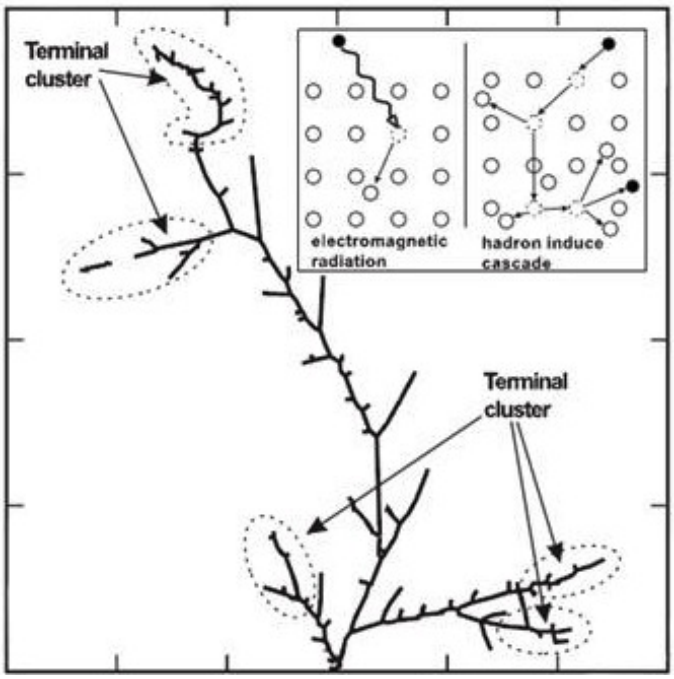

Figure 1.2 Cluster defects as a result of non-ionizing interactions

It is both these clusters as well as the previously mentioned point defects which are responsible for the bulk defects that occur within silicon. When considering neutrons and electrons, the necessary kinetic energy to produce a Frenkel pair and cluster respectively can be seen in Table 1.1.

When considering the ^{60}Co irradiations performed for this thesis, the 1.17 & 1.33

Table 1.1 Necessary energy to create bulk defects in silicon

Particle	Point Defects	Cluster Defects
Neutrons	185 eV	35 keV
Electrons	255 keV	8 MeV

MeV photons produce secondary electrons primarily by the Compton effect. Using the above photopeak energies, it can be calculate the produced electrons have a maximum energy of $\approx$ 1 MeV, which is sufficient only to create point defects and not cluster defects within the silicon. As the liberation of neutrons from photon interactions requires an incident photon energy greater than 7 MeV it can be concluded that the photons from the ^{60}Co source will not create any photoneutrons during the irradiations.

Chapter 2

Diodes and Readout System

P-type silicon semiconductor detectors have characteristics which make them ideal for small field x-ray beams in the region of approximately 1-20 MeV. This type of detector was chosen as they have a high sensitivity, small active volume and have been shown to have a stable response after being irradiated to approximately 20 kGy.

2.1 M512 Array

The Magic Plate 512 dosimeter array is comprised of 512 detectors implanted on a bulk p-type silicon substrate, this array is mounted on a 316 mm x 215 mm PCB board 1 mm thick, as seen in Fig 2.1. The array itself has dimensions of 52 mm x 52 mm with a 2 mm detector pitch. Two device configurations were used (Table 2.1):

Table 2.1 M512 Array configurations

Array #	Stop layer B-implantation μC	Substrate Resistivity Ωcm
10	100	10 (CMRP)
24	30	10 (KDB)

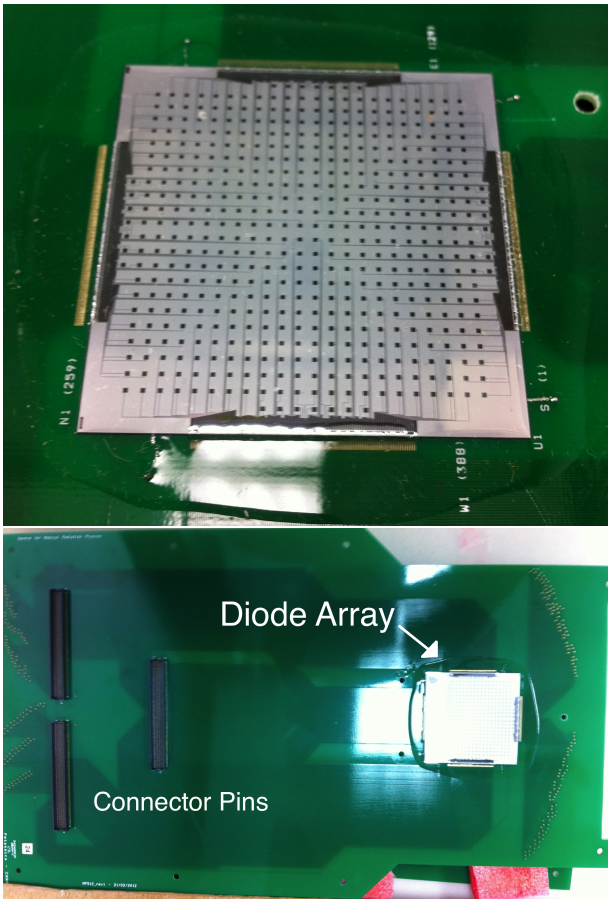

Figure 2.1 Close up of Magic Plate 512 dosimeter array and full apparatus including PCB board and connector pins

The substrate refers to the wafer substance on to which the bulk silicon is applied. The 'stop layer B-implantation' (μC) refers to the total ion charge deposited in the substrate prior to any irradiation taking place. Ionised boron is placed under the effect of an electric field and is implanted within the p-type silicon bulk with the energy of the incident boron particles at 67 keV giving a 0.08 μm depth of interaction. This process is undertaken to avoid the effect of the build up charge in the thick field oxide that can produce inverse channels on the diode surface. These inverse channels occur when two seperate n+ top junctions are present on a p-type substrate. The oxide between the junctions accumulates a naturally positive charge which in turn attracts a negative charge from the silicon substrate at the silicon/oxide interface.This negative

accumulated charge generates a conductive channel (inverse channel) of the same type as the n+ junctions, which acts as a short circuit, ruining the charge collection efficiency and electric field distribution.

For the three dose implantation values used in this thesis for both the M512 arrays and the test structures, we calculate the following dopant concentrations:

- 10 μC = 7.74 x10^{19} particles/cm^3
- 30 μC = 2.32 x10^{20} particles/cm^3
- 100 μC = 7.74 x10^{20} particles/cm^3

2.2 Test Structures

The test structures, supplied by the CMRP microelectronics foundry, are a silicon detector produced on the same wafer as the M512.

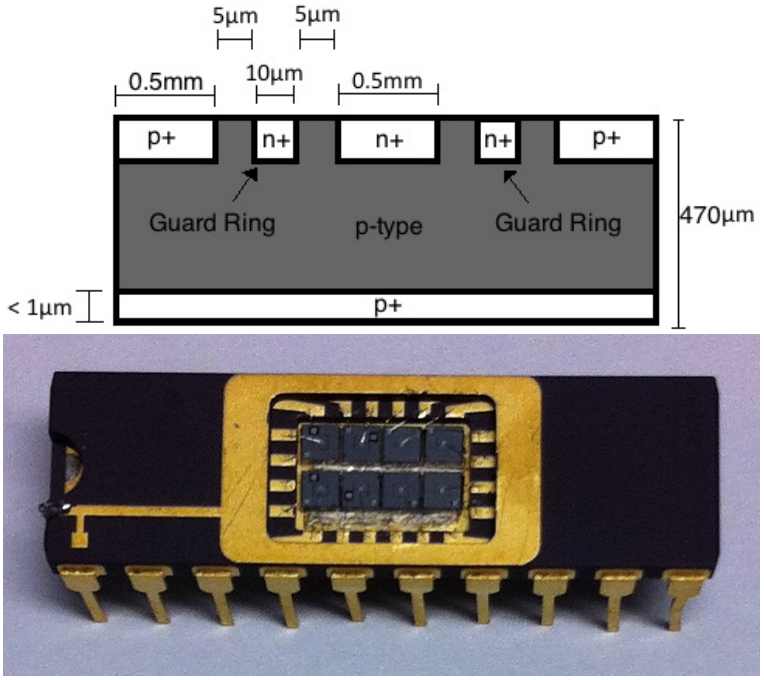

Figure 2.2 8 mounted diodes, each with individual guard rings

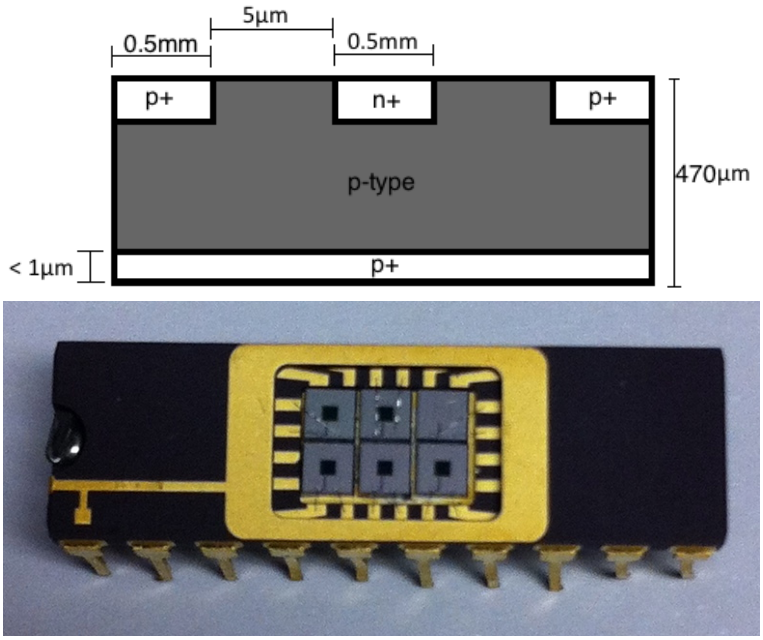

Figure 2.3 6 mounted diodes, each with no guard ring

Two versions of the test structures were utilized, one with an n^+ guard ring 10 μm in width (Fig2.2), 5 μm from the edge of the anode and one without a guard ring (Fig2.3). The guard ring is an n^+ implantation which is placed in close proximity to the n^+ to reduce the effect of the electric field created within the diode.

In order to determine which substrate and pre-irradiation dopant implantation combination would best suit the use of silicon detectors for clinical use, a range of samples were supplied with pre-irradiation dopant implantations of 10 μC, 30 μC and 100 μC. Two different types of substrates have been investigated, a 1 Ωcm and 10 Ωcm substrate from the CMRP foundry and a 10 Ωcm substrate from the KDB foundry. The test structures were placed in dual in line (DIL) ceramic packages in groups of either 6 or 8 with planar diodes on a common substrate.

2.3 TERA Chip

Figure 2.4 shows a schematic diagram of the readout system used in all diode response tests. The dotted line box represent the TERA chip, with all components inside the box part of the TERA device. The TERA device was designed by the Torino Division from the National Institue for Nuclear Physics (INFN) as an application specific integrated circuit (ASIC).

When an interaction occurs within the sensitive volume of the detector, charge is generated by the creation of electron/hole pairs and is swept up by diffusion outside of the depletion region and drift inside of the depletion region. This produces a current pulse which charges the capacitor connected in parallel with the charge-frequency converter. The charge is accumulated on a feedback capacitor until the charge accumulated in the capacitor generates a potential equal to V_{ref}. A logical pulse is then generated and counted by a digital counter, with one count corresponding to a quantum charge. Multiplying the number of counts for the quantum charge, we can calculate the total charge generated by the radiation in the detector. The instantaneous current can also be determined as a result of knowing the integration time.

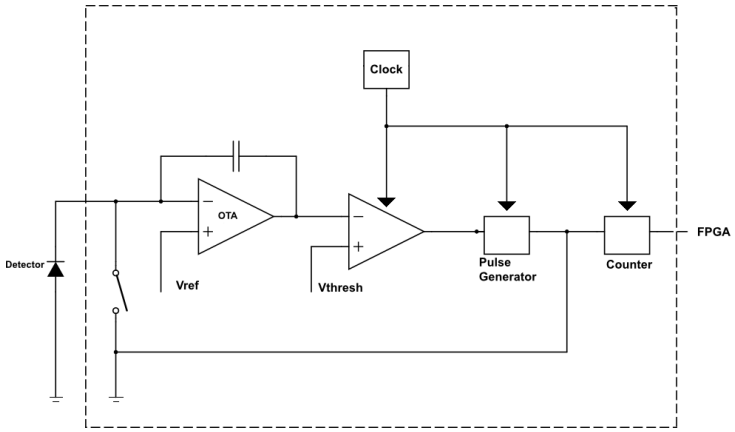

Figure 2.4 TERA chip readout system schematic

This positive signal is then sent to the pulse generator, which acts so as to produce no

pulse if an incoming signal is negative and produce a square pulse when the incoming signal is positive, this pulse is registered by the counter, and the data sent to the FPGA (field programmable gate array). The FPGA is responsible for data communication between the TERA and USB interface, and for sending commands by a software GUI. The pulse generator sends a second pulse in conjunction with the one sent to the counter, this second pulse resets the capacitor, indicating data transmission is complete, resetting the system for the next interaction event.

The whole process is undertaken with direction from the internal clock, this is so no component will trigger until so directed by the clock, ensuring there is no mixing of signals and that the entire process only registers a single event at a time. The total number of pulses is directly proportional to the incident energy on the detector.

2.4 Data Acquistion

Figure 2.5 shows the layout of the Rad-X Doseview software which was utilized in order to acquire all diode response data, the software was developed by the Centre for Medical Radiation Physics (CMRP). The Rad-X Doseview interface allows the user to see the real time response of up to 128 individual detectors as well as their respective integral response over the set time of acquisition.

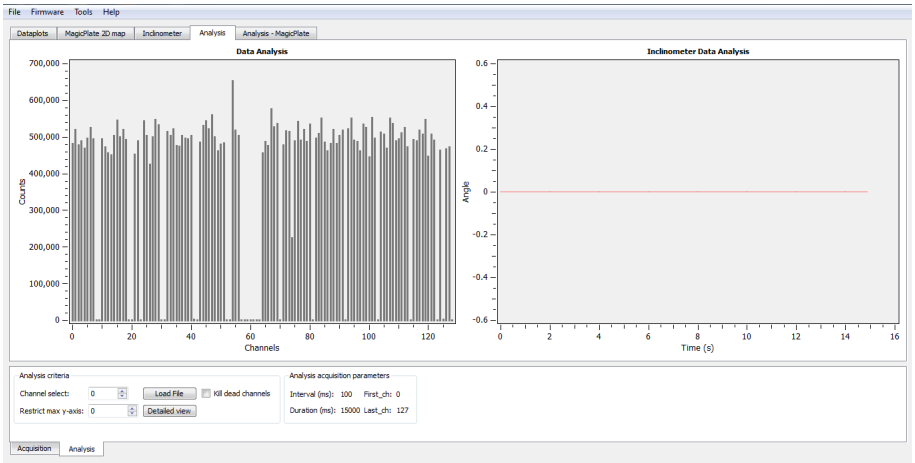

Figure 2.5 Rad-X Doseview Software with individual detector readout

Alongside the realtime numerical data for individual detectors, the software allows for a viewing of an array of devices with a dynamic relative colour based scale (Fig 2.6) to differentiate the response of detectors based on the geometry of an array. Along with the real-time data response, the software saves each acquisition to a pre-determined location which can then be post-processed for calculations, such as total dose, dose rate and timing behavior of the input signal. It should be noted that the acquisition shown in Fig 2.6 is in no way connected to the work presented in this thesis, it simply shows noise for the purpose of visualizing the software output.

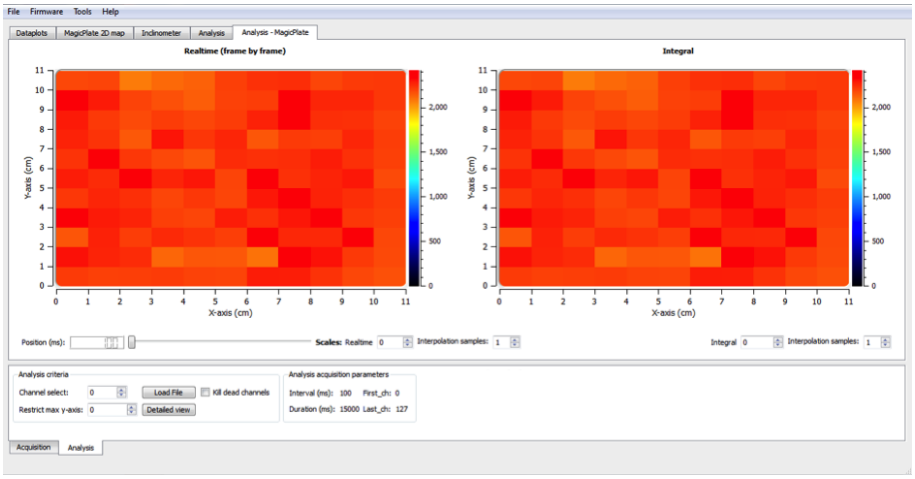

Figure 2.6 Rad-X Doseview Software for visualization of array readout

Chapter 3

Electrical Characterisation: IV and CV

3.1 IV Characteristics

Current-voltage characteristics of silicon diodes is important for determining the quality of the p-n junction. Taking into account the diode is operating in reverse bias for use as a radiation detector, the reverse (leakage) current is critical and should be considerably less than the average current produced by radiation. Leakage current relates to the operational conditions which are imposed on a diode as it is used to determine the bias voltage at which signal/noise ratio is optimum. Leakage current has two components, bulk recombination generation and surface currents.

3.2 IV Experimental Method

Current-voltage (IV) characteristics were measured using a Keithley 230 programmable voltage source to apply a bias across the diodes, a Keithley 614 electrometer & Keithley 199 System DMM/scanner to measure the current, whilst the parameters and data measurement were controlled by a custom LabView software driver.

The driver allows the definition of several parameters such as the voltage range (from 0 to -25 V in this work), incremental step amplitude (0.5 V) and delay time interval

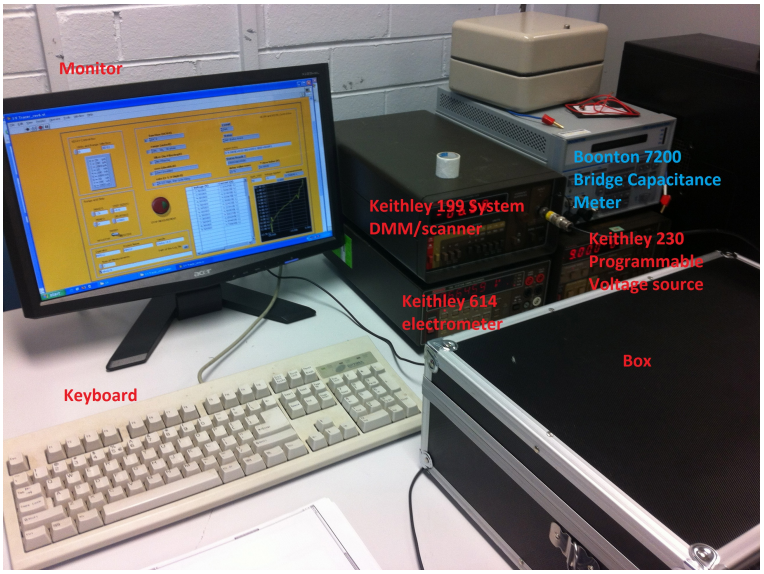

Figure 3.1 IV Characteristics Setup

between the application of the bias and the current sampling to allow for a complete stabilisation of the current transient in a large capacitance device (10 seconds in this work). All tested diodes were placed in a dark sealed container (see Fig3.1) to avoid any accidental photocurrent generation from ambient light and electromagnetic interference, they were also kept at room temperature (approximately 298 K).

Each of the data points presented in this chapter is taken as an average of all of the diodes on a particular DIL ceramic package, with the substrate resistivity and pre-irradiation ion implantation shown on the plots.

Uncertainties for all IV plots presented in this chapter are based on a 6 1/2 digit accuracy scale of the instrument used. The variable scale of the instrument was used between a range of 20 pA-200 nA, as such the uncertainties range from 0.0002-2 pA.

The diodes are operated at a reverse bias as opposed to a forward bias as silicon diodes demonstrate a far greater increase in leakage current in forward bias, as seen in Fig 3.2. Although when operated at a reverse bias, silicon diodes demonstrate a junction breakdown which does not occur in forward bias. This only occurs however at bias magnitude greater than is necessary for the operation of these particular diodes

and as such, they are to be operated in reverse bias.

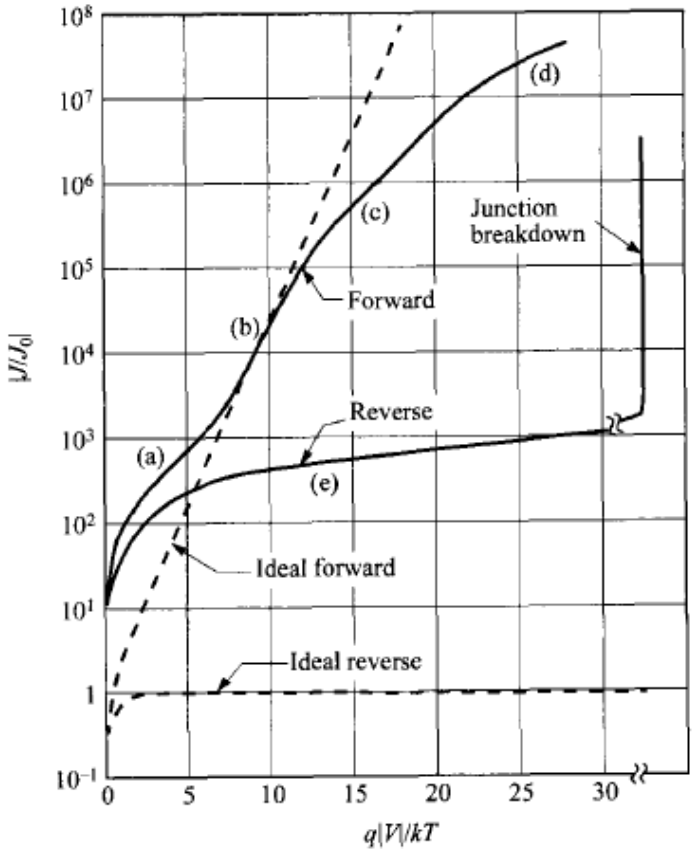

Figure 3.2 IV characteristics of a practical Si diode

Fig 3.2 [38] shows the IV characteristics of a practical silicon diode, the expected trend for the diodes used in this study under the specified conditions is labelled (e).

3.3 Experiment 1

The first IV test was undertaken on the test structure diodes of varying substrate resistivities and dose implantations which did not have a guard ring. The voltage bias was applied to the top p^+ region whilst the ammeter is connected to the n^+ region (Fig 3.3). The bias voltage applied is set from 0 V to -25 V in -0.5 V increments.

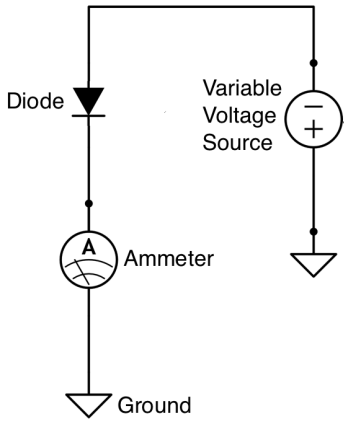

Figure 3.3 IV Experiment 1: Diodes with no guard ring connected to a variable voltage source

3.3.1 Experiment 1 Results

Figure 3.4 shows the IV characteristics for all of the test structures without guard rings. Each of the tested structures demonstrated the expected trend, although there is a considerable variation between structures with different substrates and pre-irradiation ion implantations.

Table 3.1 shows the leakage current of the samples at -25 V, the samples with the 100 μC showed the most consistent results. At a maximum negative bias of 25 V, the recorded reverse current was 33.2 pA, 46.9 pA and 53.7 pA for the 1 Ωcm(CMRP), 10Ωcm(CMRP) and 10Ωcm(KDB) substrates respectively. The samples with the 30 μC showed the highest leakage currents with the two samples tested, for the 10Ωcm(CMRP) and 10Ωcm(KDB) substrates recording a maximum leakage current of 101.49 pA and 68.9 pA respectively.

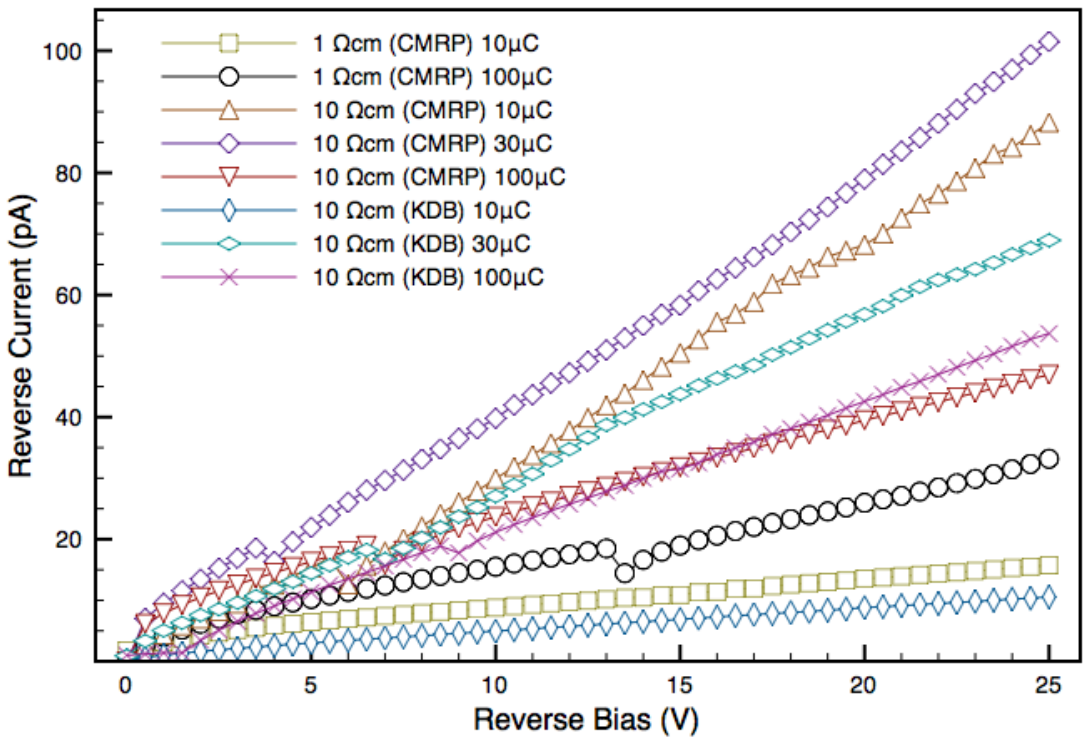

Figure 3.4 IV characteristics for all diode configurations (No guard ring)

Table 3.1 Leakage current for test structures with no guard ring

Substrate Resistivity Ωcm	Stop layer B-implantation μC	Leakage Current at -25 V pA
1 (CMRP)	10	15.73
1 (CMRP)	100	33.20
10 (CMRP)	10	88.25
10 (CMRP)	30	101.49
10 (CMRP)	100	46.9
10 (KDB)	10	10.55
10 (KDB)	30	68.90
10 (KDB)	100	53.70

A comparison of the leakage currents respective to each of the tested substrates shows the 1 Ωcm(CMRP) substrate demonstrated consistently lower leakage currents than either the 10 Ωcm(CMRP) or 10 Ωcm(KDB) substrates.

3.4 Experiment 2

The second IV test was undertaken on the test structure diodes which had a guard ring. The voltage bias was applied to the p^+ region, the ammeter is connected to the n^+ region and the IV characteristic taken when the guard ring is both grounded (Fig 3.5), and floating (Fig 3.6). Grounding of the guard ring (as per Fig 3.5) refers to the direct connection between the guard ring and a conductor attached to one side of the power supply which serves as a common return path for current for the diode, whereas floating refers to there being no direct connection between the guard ring and this conductor. The bias voltage applied is set from 0v to -25v in -0.5 V increments.

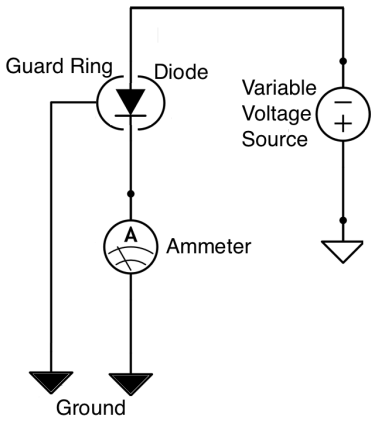

Figure 3.5 IV Experiment 2: Diode with guard ring connected to a variable voltage source with guard ring grounded

3.4.1 Experiment 2 Results

Figure 3.7 shows the IV characteristics for the samples with the 1 Ωcm (CMRP) substrate, with the guard rings both grounded and floating. The 10 μC samples showed very little deviation between the grounded and floating guard ring, although when left floating, the leakage current was consistently 1-2 pA higher than when the guard ring was grounded. The 100 μC sample demonstrated the same trend with a higher recorded leakage current when the guard ring was floating in comparison to when it was grounded. In the case of the 100 μC however, the variation between grounded

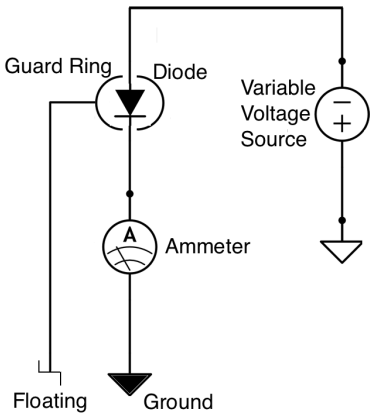

Figure 3.6 IV Experiment 3: Diode with guard ring connected to a variable voltage source with guard ring not connected to a ground

and floating was far more pronounced, with the difference between the two ranging from 10-15 pA.

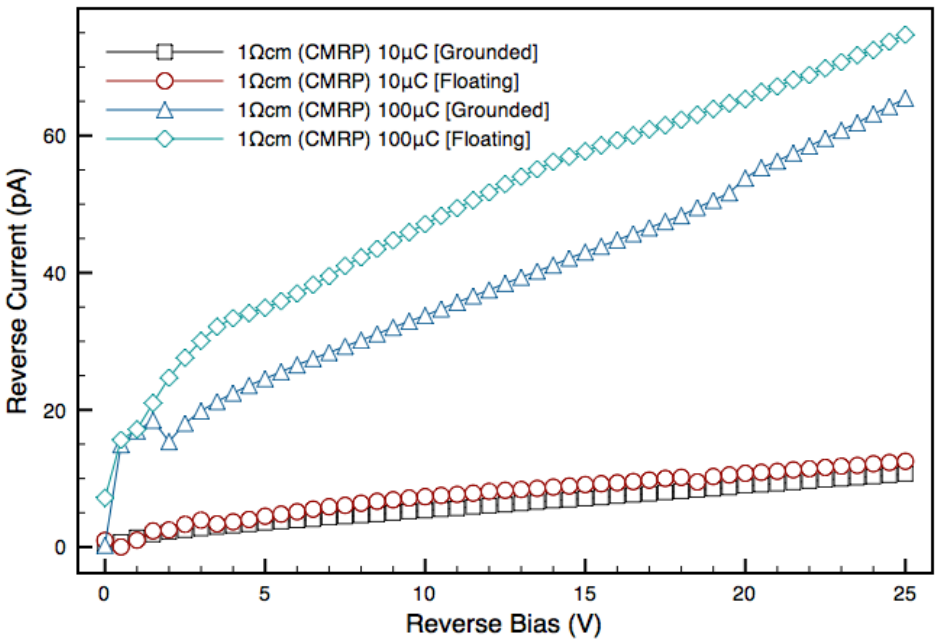

Figure 3.7 IV characteristics for 1Ωcm(CMRP) grounded and floating guard ring samples

Figure 3.8 shows the IV characteristics with guard rings both grounded and floating

for the samples with the 10 Ωcm (KDB) substrate. The 10 μC sample shows the leakage current is greater with a floating guard ring in comparison to a grounded guard ring up to a bias voltage of -20 V. At a bias voltage of -5 V, the deviation between the guard ring floating and grounded is 15 pA, this however decreases such that at -20 V we see the leakage current approximately equal. At -25 V however, the leakage current with the grounded guard ring is 2 pA higher than with the guard ring floating. The 30 μC sample shows the leakage current with the guard ring grounded in considerably lower than with the guard ring left floating, with the floating value 10-25 pA higher than the grounded. The 100 μC sample shows an opposite trend to the 10 μC sample as the leakage current is higher initially when the guard ring is grounded. By -7 V however the grounded and floating guard ring values are approximately equal, and the floating guard ring value exceeding the grounded guard ring value by 1-2 pA from -20 to -25 V.

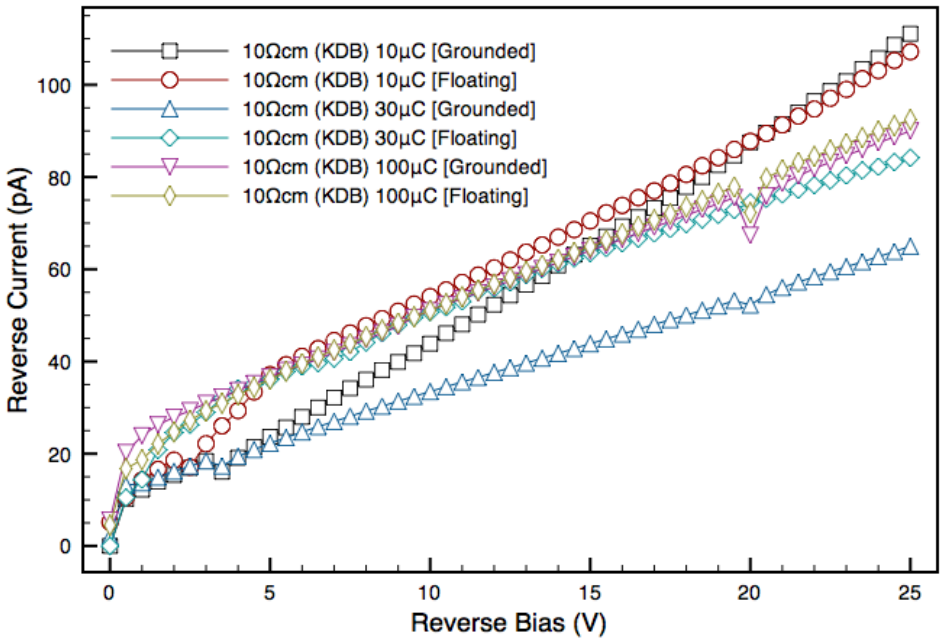

Figure 3.8 IV characteristics for 10Ωcm(KDB) grounded and floating guard ring samples

Figure 3.9 shows the IV characteristics for the samples with the 10 Ωcm (CMRP)

substrate, with the guard rings both grounded and floating. The 30 μC sample shows the leakage current with the guard ring grounded approximately 1 pA higher than the current with the guard ring floating from 0 to -4 V, the floating guard ring value is approximately 1 pA higher from -5 to 15 V, whilst from -20 to -25 V, the grounded guard ring leakage current is 4 pA higher than with the guard ring left floating.

The 100 μC sample shows the leakage current when the guard ring is grounded is consistently 1 pA higher than when the guard ring is left floating.

Results show that the effectiveness of the guard ring is strongly related to the substrate manufacturer. Suggesting that, despite the samples having the same substrate resistivity and having been processed in the same batch, the quality and purity of the substrates differs. The KDB substrate demonstrates a stronger effect of the guard ring with a stronger reduction of the superficial component of the leakage current, while for the CMRP this effect seems negligible.

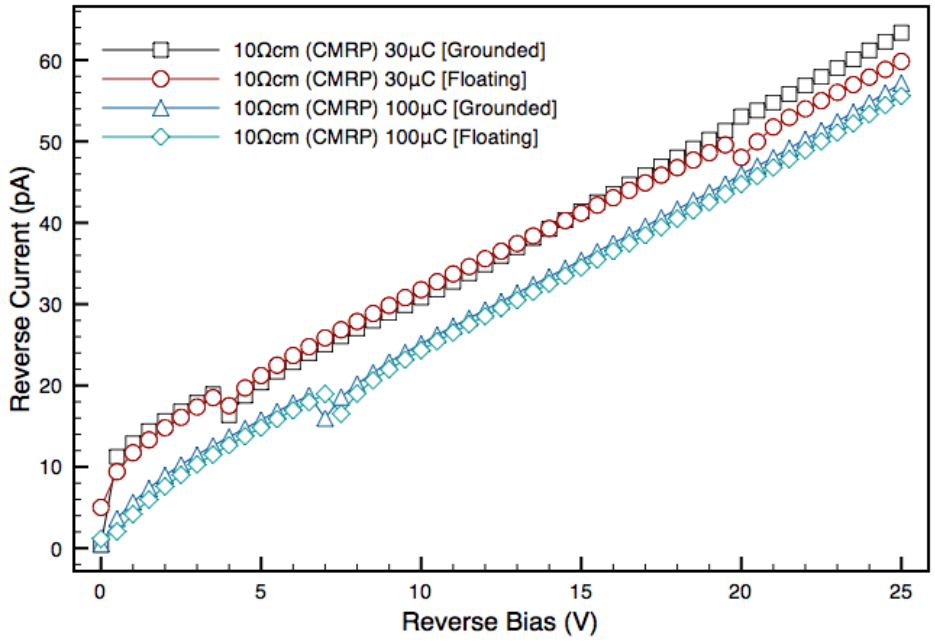

Figure 3.9 IV characteristics for 10Ωcm(CMRP) grounded and floating guard ring samples

3.5 Experiment 3

The third IV experiment was undertaken on the M512 arrays. The voltage bias was applied to one of the bias pins which is connected to a p^+ ion implanted junction on the surface of the detector, whilst the ammeter is connected to the n^+ region of each individual diode (see Fig 3.10). Unlike the test structure diodes, when undertaking IV characteristics on the arrays, there was a consistent breakdown around the -14 V bias range. The produced leakage current was outside the range of the apparatus and could not be recorded. As such the IV characteristic plots only cover a bias range from 0 V to -14 V. The bias voltage applied is set from 0 V to -14 V in -0.5 V increments.

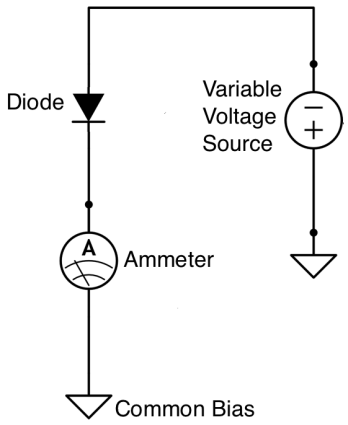

Figure 3.10 IV Experiment 3: Diodes in array individually connected to a variable voltage source (array diodes hav no guard ring)

Of the 512 diodes in the array, IV characteristics were taken on a selection of diodes in different locations throughout the array, see Fig3.11. As the geometry is the same for both of the arrays, corresponding diodes were tested on both the array structures to determine if the geometry of the device had any impact on the leakage current.

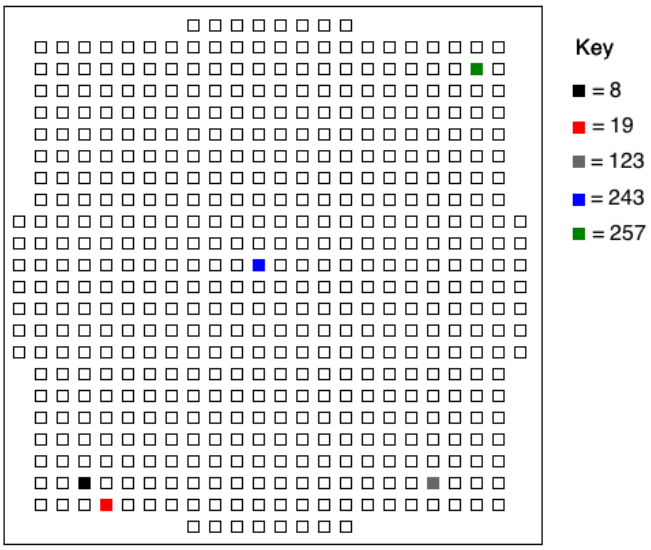

Figure 3.11 Location of tested diodes on the M512 array

3.5.1 Experiment 3 Results

Figure 3.12 shows the IV characteristics for the selected diodes shown in Fig 3.11 for Array #10 and Array #24. A logarithmic scale is used on the y-axis to better demonstrate the breakdown due to the magnitude of the leakage current at the breakdown occurs.

Examining the leakage current from the #10 array, the trend observed for all of the diodes tested is consistent up to -12 V where we observe a sharp increase in leakage current from the #8 diode; before this however, all diodes showed a gradual increase in leakage current as a function of an increase in the applied reverse bias. Diodes #19, #123 and #257 demonstrated the lowest leakage current, with a maximum current of 6, 18 and 33 pA respectively. These were noticeably lower than diode #243 which reached a maximum leakage current of 141 pA and diode #8 which rose steadily up to approximately 70 pA before the sharp increase observed at -12 V. As observed, from 0 to -12 V, the leakage current from all of the diodes from the #10 array ranges

from 1-100 pA, although this appears to be a significant deviation, these results are comparatively far better than those observed for the #24 array.

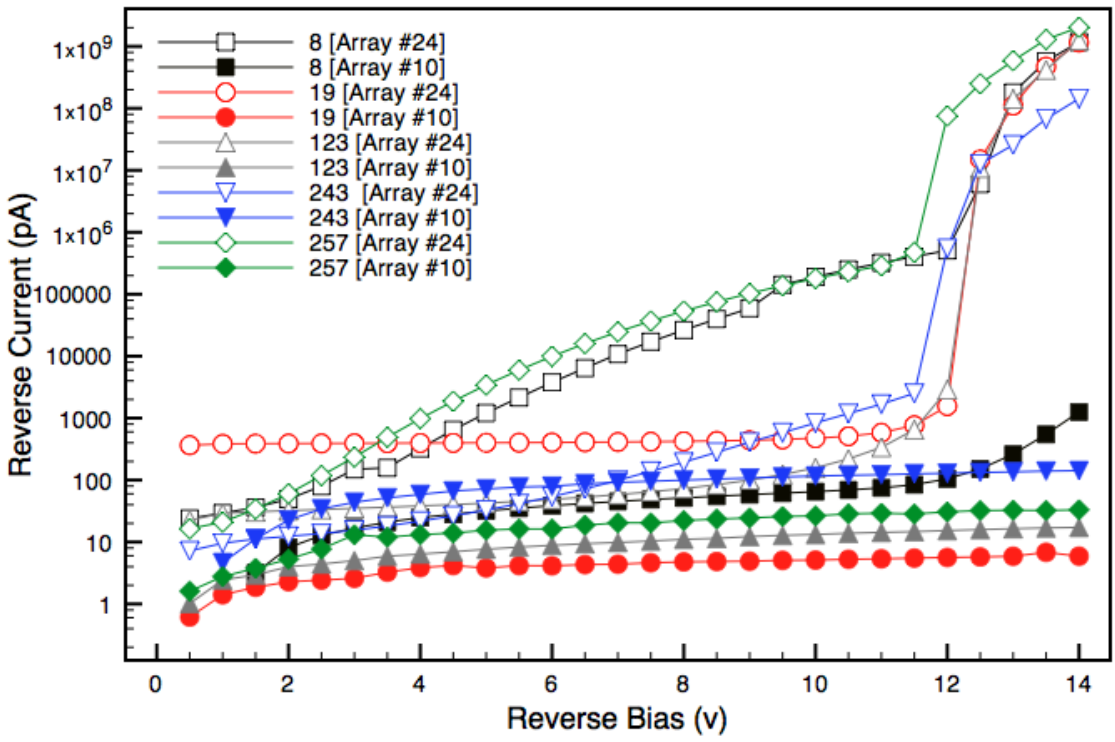

Figure 3.12 M512 IV characteristic comparison

The leakage current observed for the #24 array was much more inconsistent than the #10 array. With the exception of the #19 diode, the leakage currents of all the diodes were consistent with those from the #10 array from 0 to -2 V, at bias' with magnitude greater than this however, large deviations were observed. There were varying trends observed with the diodes from array #24, all of which however showed a breakdown at approximately -12 V. Diode #19 showed a relatively constant leakage current, similar to the diodes from array #10, however the current was considerably higher, approximately 400 pA before breaking down at -12 V. Diodes #123 and #243 showed a gradual increase in leakage current with the increase in reverse bias, diode #243 showed a steeper increase from -7 V, whilst #123 showed a similar trend but

from -10 V, both diodes broke down at approximately -12 V. Both diodes #8 and #257 demonstrated a similar increase to diodes #123 and #243, the rate of increase however was considerably greater for diodes #8 and #257. Both diodes increased from 20 pA to 250 nA between -1 to -10 V applied bias, such that by the time a breakdown was observed at approximately -12 V.

Comparing the two substrates, it is clear that the 10 Ωcm CMRP substrate (array #10) demonstrates a considerably lower leakage current that the 10 Ωcm KDB substrate (array #24). This leads to a breakdown of the tested KDB diodes at approximately -12 V, which is not present for the CMRP substrate. Due to the relatively consistent recorded leakage current between -2 to -14 V, the CMRP substrate device can be operated at a far greater bias voltage range than the KDB device.

Comparing the results from both arrays, there is no clear relation which shows leakage current is dependent on geometrical position within the array. This demonstrates that the manufacturing process can achieve a good uniformity in terms of parameters of the planar diode across the whole 4 inch wafer, where the detector array covers almost 40 % of the whole area of the wafer.

3.6 CV Characteristics

Traditionally capacitance-voltage (CV) test are used to characterize simple bulk silicon diodes for the purpose of determining the depletion bias. The depletion bias being the voltage threshold, after which any increase in bias will cause no increase in depletion width, causing capacitance to be almost constant.

In this work however, the devices used are more complicated than a simple n+/p/p+ parallel junction device (see Sec 3.2) and as a result, the interpretation of a CV plot becomes more difficult. This is due to multiple depletion steps which occur when the polarisation is changed across the contacts. It is still necessary to undertake CV characteristics of increasingly complex devices to determine the 'small signal' behavior of the device and its impact on pre-amplifier noise.

Capacitance of the detector affects the noise of spectroscopy set-up and amplitude of the charge on the input of the pre-amplifier. This is due to charge sharing between instrinsic capacitance of the pre-amplifier and the detector. According to Knoll [39] a good quality pre-amplifier used with silicon detectors may have a noise figure of 1.6 keV with zero input capacitance, but this figure may double if the input is loaded with 100 pF.

3.7 CV Experimental Method

The capacitance-voltage (CV) characteristics were measured using a Boonton 7200 Bridge Capacitance Meter, which imposed a 1 MHz sinusoidal wave onto the low detector input. This allows the capacitance to be determined through the use of two phase sensitive detectors. The maximum & minimum voltages (-60v & 0 V), step size (-0.5 V) and delay (1000 ms) are all able to be set using the LabView software which, as with the IV characteristics allows for real time data to be displayed, stored and plotted.

Using the same apparatus, three separate experiments were undertaken;

- CV characteristics on diodes with no guard ring
- CV characteristics on diodes with guard ring grounded
- CV characteristics on diodes with guard ring floating

Uncertainties for all CV plots in the remainder of this chapter are based on a 3 1/2 digit accuracy scale of the instrument used. The scale was set to pF with two decimal places recorded, as such the uncertainty for each data point is 0.005 pF.

3.8 CV Experimental Results

Figure 3.13 shows the CV characteristics of the test structures with no guard ring. In all of the devices we observe the expected trend with a maximum capacitance with no applied bias and a gradual decrease as the magnitude of the negative bias is increased.

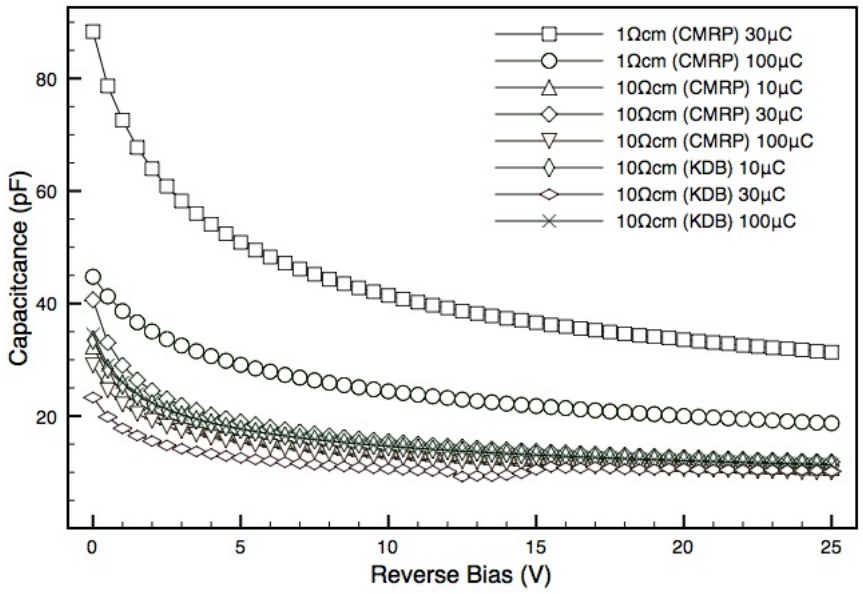

Figure 3.13 CV Characteristics of test structures with no guard rings

Examining the two 1 Ωcm substrate samples, it is clear that the response was comparatively higher than the two 10 Ωcm substrates. The 1 Ωcm sample with the 30μC ion implantation demonstrated a capacitance of 88 pF at zero applied bias which decreased to a minimum value of 32 pF at -25 V. The 1 Ωcm sample with the 100μC ion implantation demonstrated lower initial capacitance, with a maximum value of 45 pF at zero applied bias and a minimum value of 20 pF at an applied bias of -25 V.

The results for the tested structures with both the CMRP and KDB 10 Ωcm substrates were all quite similar and all followed the expected trend. The initial capacitance for the sample with the 10 Ωcm (CMRP) and 30μC ion implantation was 40 pF,

whilst for the sample with the 10 Ωcm (KDB) and 30μC ion implantation the initial capacitance was 25 pF. With the exception of these two samples, the remaining four tested structures with a 10 Ωcm substrate all demonstrated an initial capacitance from 29-34 pF. As the magnitude of the reverse bias was increased, a convergence was observed such that by an applied bias of -25 V, all of the structures with a 10 Ωcm substrate recorded capacitance value from 10.2-11.8 pF.

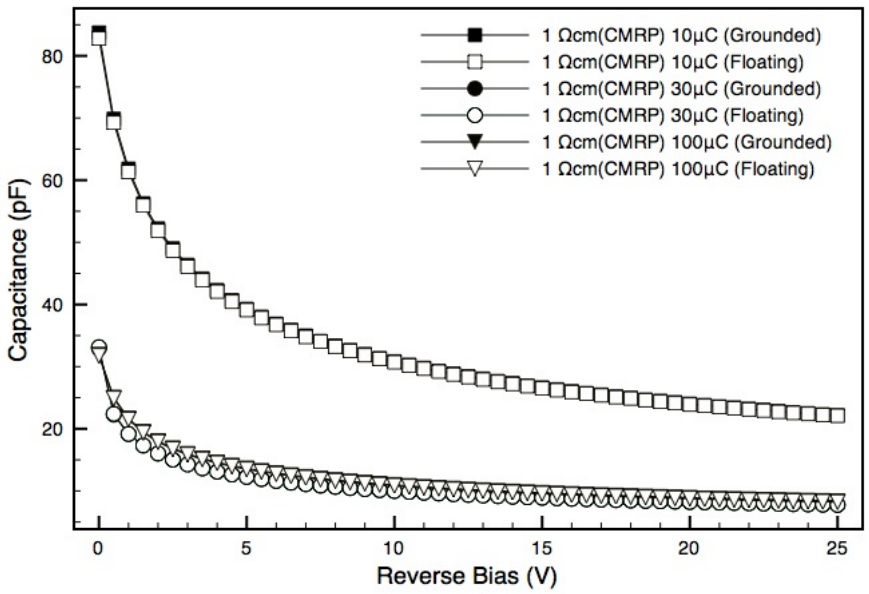

Figure 3.14 CV Characteristics of test structures with guard ring & 1 Ωcm(CMRP) substrate

Figure 3.14 shows the CV characteristics of the samples with the 1 Ωcm(CMRP) substrate and a guard ring, with the guard ring both grounded and floating as was expected. From the plot it is difficult to make any distinction between capacitance when the guard ring is grounded and when it is floating. From the plot however, it is clear that the capacitance of the sample with the 10μC ion implantation is considerable higher than the 30μC and 100μC samples.

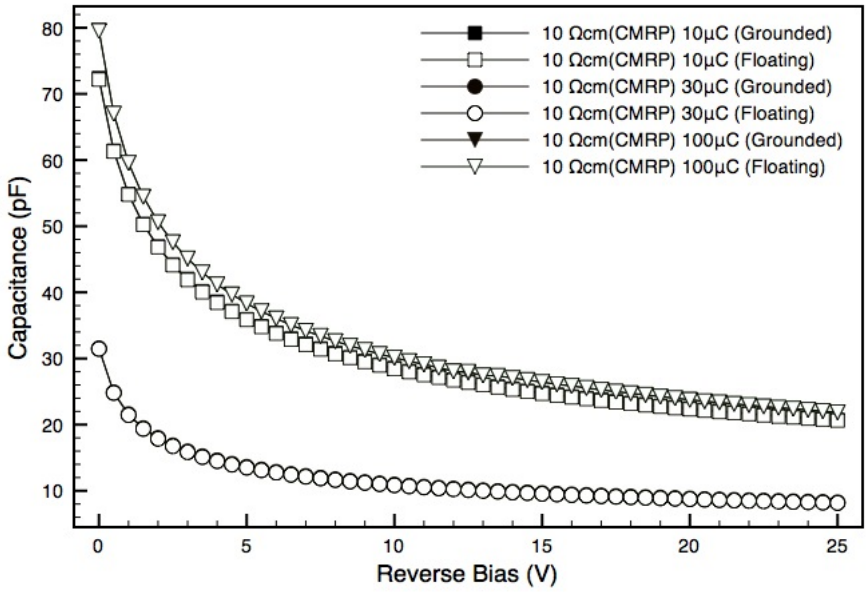

Figure 3.15 CV Characteristics of test structures with guard ring & 10 Ωcm(CMRP) substrate

Figure 3.15 shows the CV characteristics of the samples with the 10 Ωcm(CMRP) substrate and a guard ring, with the guard ring both grounded and floating. Similar to the samples with the 1 Ωcm(CMRP) substrate, it is difficult to see any difference between the capacitance when the guard ring is floating and when it is grounded. The sample with the 30μC ion implantation however does show a considerably lower capacitance than both the 10μC and 100μC samples.

Figure 3.16 shows the CV characteristics of the samples with the 10 Ωcm(KDB) substrate and a guard ring, with the guard ring both grounded and floating. As was the case with the other two substrates, it is difficult to see a distinction between the grounded and floating guard ring. The KDB substrate however shows far more consistent results than the two CMRP substrates, although we do see a deviation of 5 pF at zero applied bias between the 30μC (34.5 pF) and the 10μC (29.5 pF) and 100μC (34 pF) samples, by an applied bias of -2 V, this deviation is reduced to approximately 1 pF.

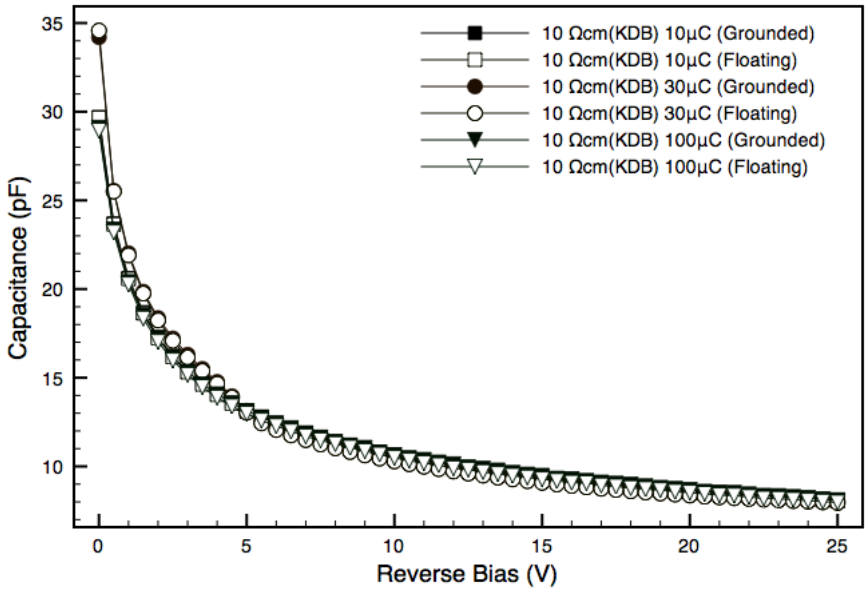

Figure 3.16 CV Characteristics of test structures with guard ring & 10 Ωcm(KDS) substrate

3.9 Summary

The aim of the IV characterization was to determine the quality of the substrate and process performed for the production of the M512 on different substrates and doping concentration of the p+ junctions. This has been performed by means of static characterisation of the test structures and then the final M512 array assembled on a thin flexible PCB carrier by wirebonding connections.

Based on the results by Theil [40], when considering boron implantation of silicon, for Experiment 1 we would expect to see a decrease in leakage current with the increase of doping concentrations. Although the 100 μC samples were the most consistent, for both the 1 Ωcm(CMRP) and 10 Ωcm(KDB) substrates, a sample with an ion implantation lower than 100 μC produced the lowest leakage current. This may indicate that the higher dose of boron implantation is improving the properties of the p-stop layer, whilst producing more radiation defects and mechanical stress on the surface of wafers that were not fully annealed. This may effect the increasing of

leakage current with dose implantation.

Experiment 2 showed inconsistent results regarding the effect of the guard ring on the leakage current of the test structures. Results by Mishra et.al. [41] reported lower leakage current for guard ring devices when the guard ring was grounded in comparison to when it was left floating. The results from the 1 Ωcm(CMRP) devices were consistent with Mishra's results as for both tested structures, the leakage current was lower when the guard ring was grounded. The test structures with the 10 Ωcm(CMRP) and 10 Ωcm(KDB) substrates did not produce results which agree with Mishra et.al. although the deviations between grounded and floating guard rings for individual test structures when they did not agree with this trend is no greater than 2 pA. Less efficiency of the 10 Ωcm test structures with the guard ring can be explained by large lateral depletion of the reverse biased diode, leading to overlapping of depletion regions of the n+ core and the n+ guard rings. More detailed analysis of this planar complicated structure is required using technology computer aided design (TCAD).

The results from Experiment 3 agreed with those of Experiment 1 as the #10 array (with 10 Ωcm(CMRP) substrate and 100 μC ion implantation) produced consistently lower leakage currents than the #24 array (with 10 Ωcm(KDB) substrate and 30 μC ion implantation). This result also agrees with the results by Theil as the diode/array with the higher dose implantation produced the lower leakage current. We can see discrepancies between these results and those from Experiment 1, as the test structure diodes with the 10 Ωcm(KDB) substrate did not demonstrate the breakdown observed at -12 V. This may be the result of defects within the bulk silicon or as a result of the geometry of the array itself.

The aim of the CV component of the experiment was to determine the capacitance of the silicon test structure devices to determine their small signal behavior.

It was determined from Fig 3.13 that with the exception of the two test structures with the 1 Ωcm(CMRP) substrate, there was very little difference between the capacitance

of the other test structures. The results for the structures with both the CMRP and KDB 10 Ωcm substrates are inconclusive, although this trend is clearly visible for the 1 Ωcm(CMRP) structures with the 30 μC structure recording approximately double that of the 100 μC structure.

The results from the guard ring comparison experiment show that the effect of grounding the guard ring has little to no effect on the capacitance of the diodes. Across the nine substrate and pre-irradiation ion implantation combinations, the maximum deviation between floating and grounded guard rings was 1 pF. This represents a deviation of $\approx$ 1-3% of the capacitance across all the samples tested and as such, would have minimal impact on any noise in a readout system.

As mentioned previously, Knoll [39] states that increased capacitance of a device will cause an increase in detector noise. The figures stated by Knoll refer to a 'good' noise figure being in the region of 1.6 keV with zero input capacitance, with an input loaded with 100 pF generating in the region of 3.2 keV. With the exception of the samples with the 1 Ωcm(CMRP) substrate with no guard ring, all of the other samples (guard ring and without) had a capacitance less than 40 pF at a voltage bias of -5 V. As such, although there was a considerable variation in the capacitance of the sample variations tested, with the exception of the 1 Ωcm(CMRP) substrate with no guard ring all samples fall within a region where the noise is considered to be acceptable.

Chapter 4

Radiation Damage for Test Structures

The purpose of a damage characterisation test is to determine the changing of the sensitivity of dosimetric devices with accumulated dose. For intensity modulated radiation therapy, the approximate water equivalent dose a p-type silicon device will receive annually is in the range of 100-200 kGy.

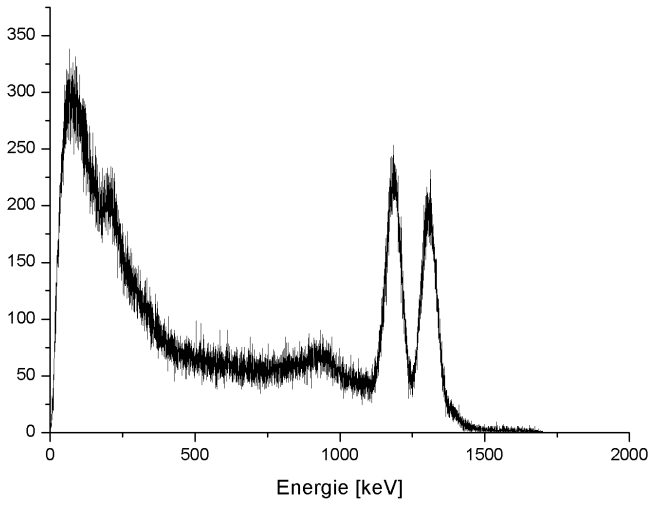

Figure 4.1 Energy spectrum of Cobalt 60

Diode irradiations were undertaken using the Gamma Technology Research Irradiator (GATRI) at the Australian Nuclear Science and Technology Organisation (ANSTO) facility at Lucas Heights. GATRI utilizes a ^{60}Co source and is able to deliver a dose

Table 4.1 Test structure irradiations

Sample	Stop layer B-implantation μC	Dose kGy
1 Ωcm(CMRP)	30	30
1 Ωcm(CMRP)	100	10
10 Ωcm(CMRP)	10	10
10 Ωcm(CMRP)	30	20
10 Ωcm(CMRP)	100	10
10 Ωcm(CMRP)	100	40
10 Ωcm(KDB)	10	20
10 Ωcm(KDB)	10	30
10 Ωcm(KDB)	30	20
10 Ωcm(KDB)	30	30
10 Ωcm(KDB)	100	10
10 Ωcm(KDB)	100	40

rate varying from 0.1-4 kGy/h [42]. The energy spectrum of ^{60}Co shown in Fig4.1, has a low energy shoulder from 0-250 keV, a plateau region from approximately 250 - 1100 keV, with the main feature of the spectrum being two large photopeaks with energies 1.17 & 1.33 MeV respectively. As such, the mean energy of the ^{60}Co energy spectrum is 1.25 MeV as an average of the two main photopeaks. All of the test structures were irradiated to either 10, 20, 30 or 40 kGy water equivalent dose, as shown in table 4.1.

Clinical treatments utilizing an x-ray beam with energies greater than 7 MeV can produce photoneutrons due to photon interaction with high Z materials in the jaws and primary collimators. These liberated photoneutrons have the ability to increase the dose to both a patient and dosimetric devices and as such must be calibrated for.

For all plots presented in this chapter, each data set comprises of the average of three repeated measurements using the same parameters. The uncertainties were calculated using the ratio of the standard deviation to the average across these three repeated measurements for each data point represented. This ratio was then multiplied by the percentage response of the data point represented to the pre-irradiation response to account for normalisation.

4.1 Photon Damage - Experimental Method

All diode response tests were undertaken at the Illawarra Cancer Care Centre (ICCC) located at Wollongong Hospital. These tests were undertaken to determine the effect of the ^{60}Co irradiations at ANSTO. The diodes were placed on the patient couch within a 30 x 30 cm^2 solid water phantom and irradiated under the following parameters:

- 100 cm Source to Surface Distance (SSD)
- 20 cm x 20 cm field size
- 6 MeV Beam using a Varian 2100C linear accelerator
- Depth = 15mm (d_{max}) in a solid water phantom
- 600 MU/minute
- 100 MU delivered
- 100 mm solid water backscatter

Solid water, is a water equivalent material designed by CNMC for dosimetric calibrations to within 1% of a true water dose.

MU (Monitor Unit) is a measure of linear accelerator output, with 100 MU being proportional to an absorbed dose of 1 Gy delivered to d_{max} in a water equivalent phantom whose surface is at the linear accelerators isocentre.

An initial pre-irradiation response was recorded for each diode as well as a post-irradiation response which is normalised to the 0 dose data. Data acquisition in all cases was undertaken by the Rad-X Doseview data acquisition system.

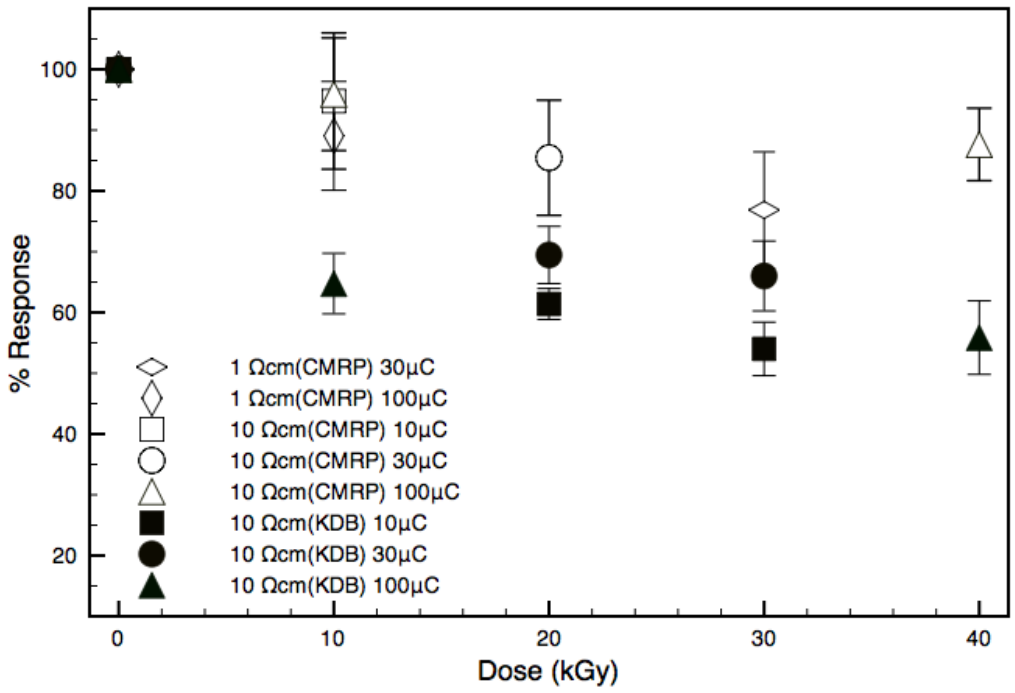

Figure 4.2 Relative response change as a result of photon damage

4.2 Photon Damage Results

Figure 4.2 shows the relative response change for test structures with the 1 Ωcm and 10 Ωcm CMRP substrates as well as test structures with the 10 Ωcm(KDB) substrate. All diodes demonstrated the expected trend of response decrease with accumulated dose.

The sample with the 1 Ωcm(CMRP) and 100 μC ion implantation showed a percentage response of 90% after being irradiated to 10 kGy whilst the sample with the same ion implantation with a 10 Ωcm(CMRP) substrate demonstrated a 95% response for the same accumulated dose. The sample with the 1 Ωcm(CMRP) and 30 μC ion implantation showed a 77% response after an accumulated dose of 30 kGy. Comparitively the sample with the same ion implantation and the 10 Ωcm(KDB) substrate demonstrated a 66% response for the same dose.

The test structures with the 10 Ωcm(CMRP) demonstrated consistently the smallest response decreases. The 10 Ωcm(CMRP) 100 μC sample showed a 95% response after a 10kGy irradiation whilst the 100μC sample with the 10 Ωcm(KDB) substrate demonstrated a 65% response for the same dose. Similarly these same two samples returned a response of 88% and 56% respectively for an irradiation of 40 kGy. The same trend is evident with the samples with the 30 μC ion implantation which, for a dose 20 kGy returned percentage responses of 85% and 69% for the 10 Ωcm(CMRP) and 10 Ωcm(KDB) substrates respectively.

Considering the samples with the 10 Ωcm(CMRP) substrate, we can see that at 10 kGy, the 100 μC sample decreases less than the 10 μC sample. The 100 μC sample at 40 kGy also shows a smaller decrease than the 30 μC sample at 20 kGy. For the samples with the 10 Ωcm(KDB) substrate we can see this same trend with both 20 & 30 kGy where the 30 μC samples demonstrate a higher percentage response than the 10 μC samples. Despite the 100 μC sample at 10 kGy not fitting this trend, we can assume that a higher implantation dose helps to minimise the charge collection reduction due to the radiation damage induced by gamma particles. The estimated pre-irradiation dose for the KDB substrate is approximately 40 kGy to stabilise the response of the detector at 59%. For the CMRP substrate, even if the response decrease is small compared to the KDB substrate it seems to be still fluctuating after 40kGy as suggested by the large error bars obtained for these samples.

4.3 Photoneutron Damage - Experimental Method

The method by which we determined the effect of photoneutrons on silicon detectors in a clinical environment was to irradiate them for a prolonged period of time using an 18 MeV beam. The initial response of the detectors was undertaken at the ICCC using a 6 MeV beam as explained previously, this was used as a reference by which the irradiated detectors could then be compared and the response normalised.

The irradiation was undertaken at St George Hospital using the following parameters;

- 100 cm SSD (Source to Surface Distance)
- 40 cm x 40cm field size
- 18 MeV beam using a Varian iX linear accelerator
- Depth = 0 mm (Surface test)
- 600 MU/minute
- 9795 MU delivered
- 130 mm solid water backscatter

These linac irradiation parameters differ from that of the photon damage response tests in as the purpose is to liberate photoneutrons rather than determine the changing response as a result of accumulated dose. The field size is increased to 40 cm x 40 cm to generate the largest possible number of photoneutrons as well as decreasing the necessary exposure time. The increased dose was chosen as a result of the field size to achieve an approximate equivalent dose of 300 Gy.

One test structure was also irradiated to the same parameters but placed at a depth of 40 mm (d_{max} for an 18 MeV beam) within a solid water phantom.

After this irradiation, the diodes were taken back to the ICCC and response tests were undertaken using the same parameters as stipulated for the photon damage experiment.

4.4 Photoneutron Damage Results

Figure 4.3 shows the relative response decrease of five samples which were irradiated using an 18 MeV beam. From the plot we can see a clear trend emerging with the 10Ωcm(CMRP) substrate performed consistently better than the 10 Ωcm(KDB) samples. It is also evident from the plot that the pre-irradiation ion implantation

affects the relative response change as for each substrate we see that the lower the dopant concentration, the greater the relative response decrease.

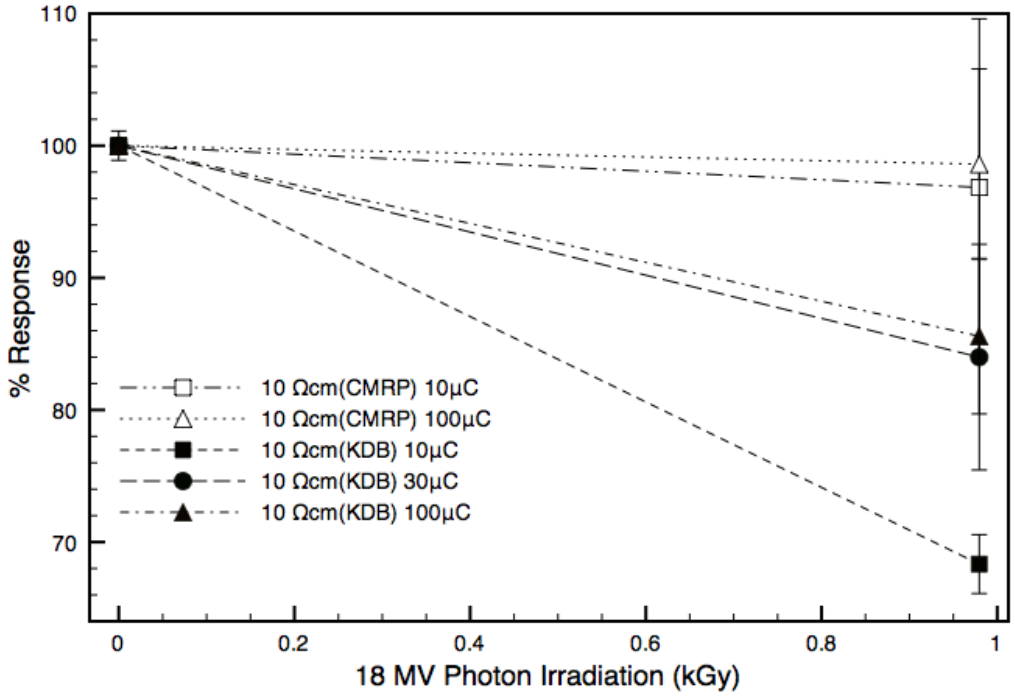

Figure 4.3 Relative response change as a result of photoneutron damage

Table 4.2 Relative response changes due to photoneutron damage

Sample	Post-Irradiation Response %	Error %
10 Ωcm(CMRP) 10 μC	96.84	12.79
10 Ωcm(CMRP) 100 μC	98.60	7.21
10 Ωcm(KDB) 10 μC	68.33	2.23
10 Ωcm(KDB) 30 μC	83.79	8.54
10 Ωcm(KDB) 100 μC	85.56	5.88
1 Ωcm(CMRP) 100μC	99.21	2.21

From Table 4.2 we can see the 10 Ωcm(CMRP) 100 μC sample demonstrated a 1.4% response drop in comparison to a 14.44% drop for the sample with the 10 Ωcm(KDB) with the same pre-irradiation dopant implantation. Similarly the 10 Ωcm(CMRP) 10

μC sample demonstrated a 3.16% drop in comparison to the 31.67% response drop by the 10 Ωcm(KDB) sample with the sample pre-implantation dopant concentration.

Table 4.2 also shows data for a 1 Ωcm(CMRP) 100μC test structure which does not appear on Fig 4.3, this test structure was placed at 40 mm depth within a solid water phantom. Extrapolating using the data from Fig 4.2, it was determined that the total decrease in response observed was as a result of the photon dose, and as such the decreased response as a result of neutron dose was negligible (99.21%).

4.5 Summary

From the photon damage experiment, it can be seen that the samples with the 10 Ωcm(CMRP) substrate demonstrated a consistently smaller decrease in relative response as a result of accumulated dose. Similarly with samples from all three substrates, there was evidence to suggest an absolute relationship between response decrease and pre-irradiation ion implantation. Although this is the case the samples with the 100 μC ion implantation did demonstrate lower decreases than those samples with a smaller implantation concentration.

It is important to note that the 1 Ωcm(CMRP) samples demonstrated a greater response decrease compared to the 10 Ωcm(CMRP) samples. This is inconsistent with results by Grussell and Rikner [43] which demonstrated a decrease in substrate resistivity lead to a decrease in response change.

The results for the samples with the 10 Ωcm(KDB) substrate however agree with the literature as the 10 Ωcm(KDB) samples show a 10-20% greater response decrease than the 1 Ωcm(CMRP) samples. This suggests the KDB substrate is of higher purity, with less contaminants such as oxygen and carbon ions in comparison to the CMRP substrate, and as such the samples with the CMRP substrate demonstrated less stability with increased cumulative dose.

When considering the 18 MV irradiation to liberate photoneutrons, the same issue

arises in the small sample size, although in this case a clear trend is evident. Consistent with the photon irradiation, we see the samples with the 10 Ωcm(CMRP) substrate are less sensitive to radiation damage than the 10 Ωcm(KDB). The most prominent conclusion we can draw from this test would be the effect of the dopant implantation on the response decrease. As stated previously, the samples with the lowest dopant concentrations of 10 μC showed the greatest percentage decrease for their respective substrates. The 100 μC samples performed the best for their respective substrates with the smallest percentage decrease after irradiation. We can also conclude from the photoneutron irradiation using the 1 Ωcm(CMRP) 100 μC sample that the effect of radiation damage at depth is minimal in comparison to the photon damage.

For both photon and photoneutron damage, the test structures with the 100 μC pre-irradiation ion implantation consistently performed better than either the samples with either 10 or 30 μC pre-irradiation ion implantation. This may be due to the higher doping concentration in the p+ junction creating a higher doping gradient between the junction and the p-type substrate. The higher gradient generates a higher electric field across the p+/p/n+ junction and then a wider space charge region.

Chapter 5

Radiation Damage for Magic Plate 512 Arrays

The purpose of performing radiation damage tests on the detector arrays is that, although a similar test has been undertaken on the test structures, it is necessary to determine if the test structure and array results are congruent. With the array setup, it must also be determined if the aggregation of a large number of junctions on the same substrate will have an impact of the performance in comparison to the test structures.

All detector irradiations were performed at the GATRI facility at ANSTO using a ^{60}Co source with the arrays being irradiated to 10 kGy between each successive response test up to a total accumulated dose of 40 kGy.

5.1 Experimental Method

All diode response tests were undertaken at the Illawarra Cancer Care Centre (ICCC) located at Wollongong Hospital. The diodes were placed on the patient couch and irradiated under the following parameters:

- 100 cm SSD (Source to Surface Distance)
- 20 cm x 20 cm field size

- 6 MV Beam from a Varian 2100C linear accelerator
- Depth = 15 mm (d_{max}) in 0.5 cm bolus & 1 cm solid water, 30 mm, 50 mm & 100 mm
- 600 MU/minute
- 100 MU delivered
- 15 s acquisition
- 100 mm solid water backscatter

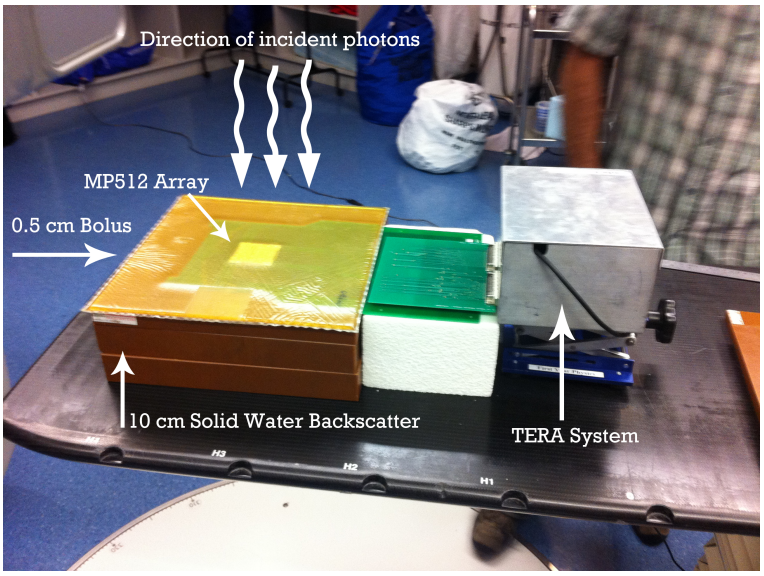

Figure 5.1 Experimental setup for M512 response tests

Uncertainties were calculated in the same manner as described in Chapter 5.

5.2 Radiation Damage Results

The test was undertaken on the the two Magic Plate 512 arrays #24 (10 Ωcm(KDB) substrate and 30 μC ion implantation) and #10 (10 Ωcm(CMRP) substrate and 100

μC ion implantation) with the results being shown in Figure 5.2 and Figure 5.3 respectively. The choice of these two samples was based on the results obtained from the test structures and to verify the best manufacturing combination of substrate type and ion implantation charge. The implantation charge of 10 μC did not show any significant advantage and so only the 30 μC and 100 μC have been chosen. The test structure based on the CMRP substrate showed in general a low response but a very small sensitivity to radiation damage for both gamma and photoneutrons, as such, we opt for the 100 μC ion implantation. The KDB substrate showed a large response corresponding to high charge collection efficiency, it did show a comparitively larger sensitivity to radiation damage. Ideally we would opt for the 100 μC ion implantation, due to technical issues during the fabrication process this was not possible, so we opted for the 30 μC ion implantation.

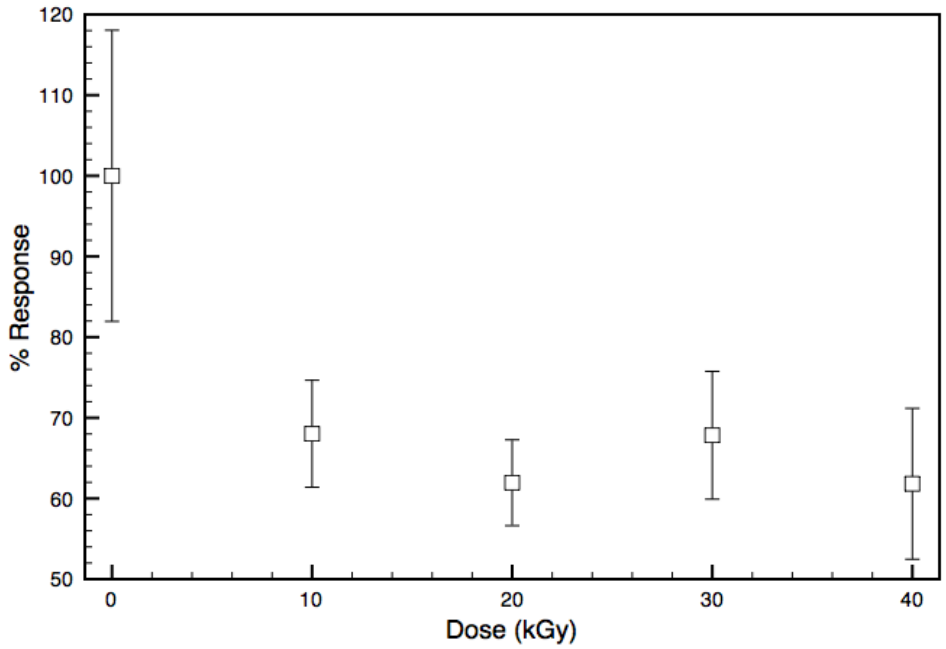

Figure 5.2 Relative response change for array #24 (10 Ωcm(KDB) substrate and 30 μC implantation) at dmax

Looking at Figure 5.2 we can see quite a substantial relative response change between the pre ^{60}Co irradiation response and the response after being irradiated up to 10 kGy.

The percentage difference in terms of relative response from pre-irradiation to 1 kGy is 31% which seems quite substantial, if we look at the responses taken at 20 ,30 & 40 kGy however, we can see that the response stabilizes within an approximate range of 10%. Although we do see an alternating increase/decrease of response as a function of total dose, each point between 10-40 kGy falls within the statistical uncertainty of the other.

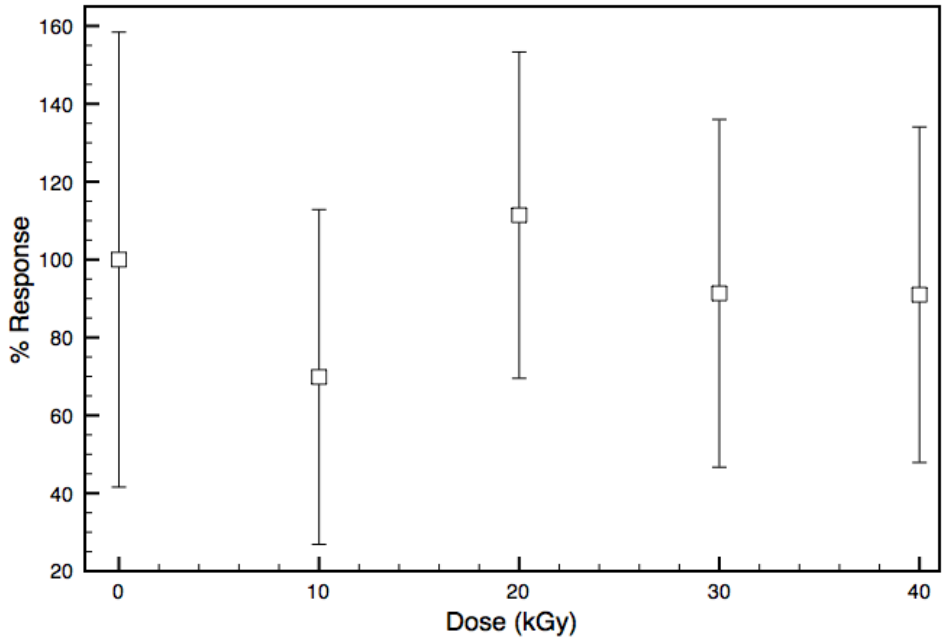

Figure 5.3 Relative response change for array #10 (10 Ωcm(CMRP) substrate and 100 μC implantation) at dmax

Looking at Figure 5.3 it is difficult to make any kind of accurate assessment regarding the relationship between dose and relative response of the array. Although the average value for each dose does seem to follow a rough linear trend, the calculated uncertainties are too large for any relevant conclusion to be made. This uncertainty is due to the absolute responsiveness of the substrate, which was in the region of 10-20 x 10^3 counts per channel for each acquisition. Comparatively, the absolute response of array # 24 with the KDB substrate was in the region of 50-70 x 10^4 counts per channel for each acquisition. This lower sensitivity appears to be related to the

quality of the substrate, strong recombination centres coupled with a lack of charge collection efficiency.

5.3 Summary

Comparing the results for array # 10 (Fig 5.3) and array #24 (Fig 5.2), array #10 demonstrated a smaller response change than array #24. Although this is the case, when we take into account the uncertainties and the absolute response of the arrays, it is clear that array #10 is unsuitable for any kind of accurate dosimetry and array #24 would clearly be the preferred dosimetry array.

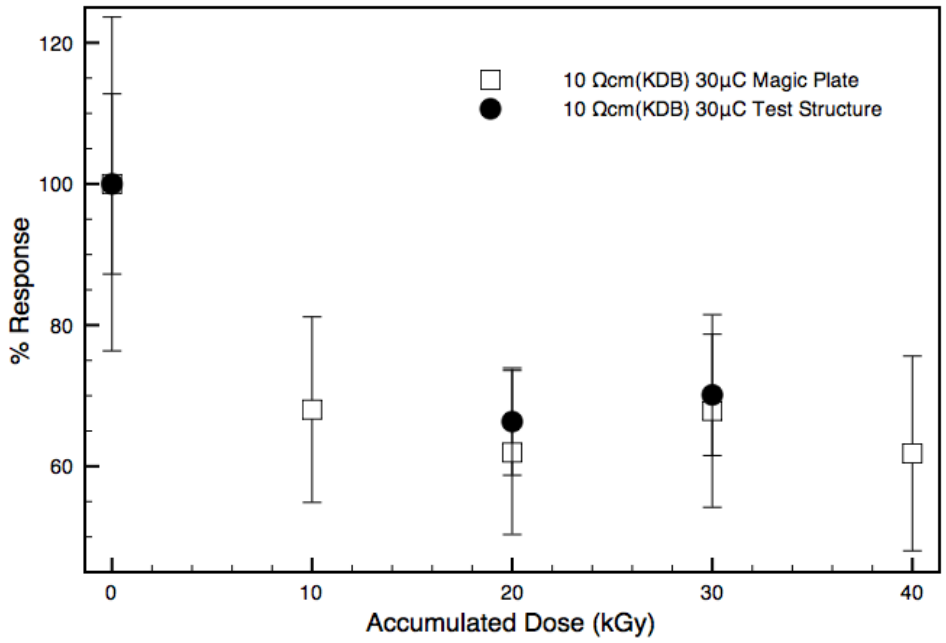

Figure 5.4 Relative response comparison of 10 Ωcm(KDB) test structures and Magic Plate

Fig 5.4 shows that the relative response data for the 10 Ωcm(KDS) Magic Plate falls within experimental uncertainty of the data for the test structures with the same substrate and dopant configuration. The test structure data shows a slightly smaller response decrease than that of the M512 array, at 20 kGy the deviation between the test

structures and the array is less than 4.5% whilst at 30 kGy the deviation is less than 2.5%. This small deviation indicates that the PCB board and array structure has little effect on the overall response of the diodes in terms of noise integrity.

The results from array #24 agree with simulations performed by Petasecca et al. [44], which simulated an n+/p/p+ silicon structure by a TCAD (Technologic CAD) radiation damage model for p-type substrates. Although these simulated a high resistivity substrate (3 kΩcm), the results demonstrated a decreased charge collection efficiency with increased fluence, which correlates with the data presented in Fig 5.3.

Considering array #10, any comparison to the test structure response of the same substrate resistivity and pre-irradiation ion implantation would be pointless as the scale of the error bars does not allow for any kind of accurate comparison.

Chapter 6

Conclusion and Future Work

The aim of this study was to characterise bulk silicon diodes for the Magic Plate 512 dosimeter array and determine the optimum substrate resistivity and pre-irradiation ion implantation for use in 4D radiation therapy. This was undertaken by studying the IV and CV characteristics as well as changing response with increased radiation damage of both test structures and the M512 arrays.

Analysis of the IV characteristics showed that for the test structures without a guard ring, there was no obvious relationship between ion implantation and leakage current. The literature suggests an increased doping concentration leads to a decreased leakage current. Although the three samples with the highest pre-irradiation ion implantation (100 μC) across the three different substrates produced the most consistent results, there were two variations with a lower pre-irradiation ion implantation which demonstrated lower leakage currents over the bias range. The comparison of test structures with guard rings demonstrated inconsistent results as some of the test structures recorded lower leakage currents with the guard rings grounded whilst others showed the opposite effect. There was no conclusive evidence that the introduction of a guard ring to the detector reduced the leakage current, this drove the decision to avoid the use of a guard ring structure in the final detector array design.

Analysis of the IV characteristics of the M512 arrays demonstrated a significantly lower leakage current for the #10 array with the 10 Ωcm(CMRP) substrate than the

#24 array with the Ωcm(KDB) substrate. The #24 array also demonstrated a breakdown at -12 V which was not present in the #10 array. The increased leakage current between the two arrays only becomes prominent when the voltage bias is increased beyond ≈ -2.5 V. This is important as in radiotherapy, most solid state detectors are used in passive mode to minimise the effect of the leakage currents.

Analysis of the CV characteristics show that the introduction of a guard ring, whether it be left floating or grounded has little impact on the capacitance of the structures. It was demonstrated in Fig 3.13 that the variations in pre-irradiation ion implantation in the test structures with a higher resistivity substrate add little effect on the capacitance . The substrate resistivity itself however presents as a much more significant variable as the two samples tested with the lowest substrate resistivity (1 Ωcm) demonstrated a considerably higher capacitance than the samples with 10 Ωcm substrate.

The results from the test structure radiation damage experiments demonstrated that for both photons and photoneutrons, the response change from the diodes with the 10 Ωcm(CMRP) substrate was consistently smaller than that of the diodes with the 10 Ωcm(KDB) and 1 Ωcm(CMRP) substrates. It is also observed that the samples with the 100 μC pre-irradiation ion implantation demonstrated a smaller response decrease on average than the samples with the 10 or 30 μC implantation.

The radiation damage tests for the M512 arrays demonstrated results consistent with the test structures in that the array #10 with the 10 Ωcm(CMRP) substrate showed a smaller response decrease than the #24 array with the 10 Ωcm(KDB) substrate. The absolute response for the #10 array however was so low that the uncertainty in the data becomes too large to make an accurate assessment of the changing response. Although the response change for the #24 array was considerably lower than #10, the accuracy of the data and the stability of the data after 10 kGy make the array far superior to #10 for accurate dosimetry.

From the data obtained it can be concluded that the CMRP substrates demonstrate the lower leakage current, significantly less when they are organised in the M512 array

format. This lower leakage current results in the data obtained using these detectors having less noise and hence, more accuracy. The capacitance of the diodes appear more dependant upon substrate resistivity than pre-irradiation ion implantation, thus a 10 Ωcm substrate, be it CMRP or KDB would be preferable for a minimised impact on pre-amplifier noise. The 10 Ωcm(CMRP) diodes demonstrated the smallest response change, although it was shown that in the array format, the absolute response of these diodes was not large enough to avoid uncertainties in the region of 50-60%. As a result of the larger absolute response and the relative stability after a 10 kGy irradiation, the #24 array (10 Ωcm(KDB) substrate), whilst showing a considerably larger response change, is comparatively a far better dosimetry device. Although this is the case, when we consider the IV data, it is important to note the breakdown which occurs at -12 V and as such, if this array is to be used as a 4DRT dosimetry device, the operating bias must be in the 0 to -4 V range in order to avoid significant increases in detector noise.

Further characterisation of array #24 is planned to determine the feasibility of the device for clinical use, with experiments related to percentage depth-dose, output factor, energy dependence and beam profiling being planned.

The detector is also going to be used in a movable phantom for characterisation of the timing performance, dose reconstruction performance when the detector is moving relative to the beam, as well as comparisons with EBT2 films.

Bibliography

[1] Keall et al. Geometric accuracy of a real-time target tracking system with dynamic multileaf collimator tracking system. *Int. J. Radiation Oncology Biol. Phys*, (5), July 2006.

[2] Woo et al. Does the peacock have anything to do with radiation therapy? *International Journal of Radiation Oncology*, (35), June 1994.

[3] J.L. Bedford and A.P. Warrington. Commissioning of volumetric modulated arc therapy (vmat). *International Journal of Radiation Oncology and Biological Physics*, (2), June 2009.

[4] A.M. Allen, M. Kristie, J. Hayman, and J.M. Balter. Evaluation of the influence of breathing on the movement and modelling of lung tumours. *Int J Radiat Oncol Biol Phys*, (4), January 2004.

[5] P. Keall. 4-dimensional computed tomography imaging and treatment planning. *Seminars in Radiation Oncology*, (1), January 2004.

[6] P. Keall, G.T.Y Chen, and S. Joshi. Timethe fourth dimension in radiotherapy (astro panel discussion). *Int J Radiat Oncol Biol Phys*, (1), January 2003.

[7] R.C. McGarry, L. Papiez, M. Williams, T. Whitford, and R.D. Timmerman. Stereotactic body radiation therapy of early-stage non-small-cell lung carcinoma: Phase i study. *Int. J. Radiation Oncology Biol. Phys.*, (4), April 2005.

[8] Frank Herbert Attix. *Introduction to Radiological Physics and Radiation Dosimetry*. WILEY-VH Verlag GmbH & Co, Weinheim, Germany, 2004.

[9] C.D Wagtner. Third international conference on radiotherapy gel dosimetry. In *The ideal dosimeter for intensity modulated radiation therapy(IMRT)*, 2004.

[10] D.A. Low, J.M. Moran, J.M. Dempsey, J.F. Dong, and M. Oldham. Dosimetry tools and techniques for imrt. *Med Phys*, (38), March 2011.

[11] Bhullar A and C. Watchman. The effective depth of cylindrical ionization chambers in water for clinical proton beams. *Physics in biology and medicine*, (1), July 2011.

[12] H. Bouchard and J. Seuntjens. Ionization chamber-based reference dosimetry of intensity modulated radiation beams. *Med Phys*, (31), July 2004.

[13] C. Martens, C. De Wagter, and W. De Neve. The value of the pinpoint ion chamber for characterization of small field segments used in intensity modulated radiotherapy. *Phys. Med. Biol*, (45), February 2000.

[14] I. Griessbach, M. Lapp, J. Bohsung, G. Gademann, and D. Harder. Dosimetric characteristics of a new unshielded silicon diode and its application in clinical photon and electron beams. *Med. Phys*, (32), November 2005.

[15] M. Westermark, J. Arndt, B. Nilsson, , and A. Brahme. Comparative dosimetry in narrow high-energy photon beams. *Phys. Med. Biol*, (45), August 2000.

[16] N. Rustgi. Evaluation of the dosimetric characteristics of a diamond detector for photon beam measurements. *Med. Phys*, (5), February 1995.

[17] N. Rustgi. Diamond detector versus silicon diode and ion chamber in photon beams of different energy and field size. *Med. Phys*, (8), May 2003.

[18] J. Troncalli and J. Chapman. Tld linearity vs. beam energy and modality. *Med. Dosim*, (4), December 2002.

[19] I. Pai, J. Das, J.F. Dempsey, K.L. Lam, T.J. Losaso, A.J Olch, R. Palta, L.E. Reinstein, D.Ritt, and E.E. Wilcox. Tg-69: Radiographic film for megavoltage beam dosimetry. *Med. Phys*, (5), April 2007.

[20] T. M. Bogucki, W. R. Murphy, C. W. Baker, S. S. Piazza, and A. G. Haus. Processor quality control in laser imaging systems. *Med. Phys*, (4), January 1997.

[21] L. McLaughlin, C. G. Soares, J. A. Sayeg, R. W. Kline E. C. McCullough, A. Wu, and A. H. Maitz. The use of a radiochromic detector for the determination of stereotactic radiosurgery dose characteristics. *Med. Phys*, (3), October 1994.

[22] L. McLaughlin, C. G. Soares, J. A. Sayeg, E. C. McCullough, R. W. Kline, A. Wu, and A. H. Maitz. Dosimetric evaluation of gafchromic xr type t and xr type r films. *Appl. Clin. Med. Phys*, (1), April 2005.

[23] D. A. Low, J. F. Dempsey, J. Markman, S. Mutic, E. E. Klein, J. W. Sohn, and J. A. Purdy. Toward automated quality assurance for intensity modulated radiation therapy. *International Journal of Radiation Oncology and Biological Physics*, (2), June 2002.

[24] Y. El-Mohri, L. E. Antonuk, J. Yorkston, K.-W. Jee, M. Maolinbay, K. L. Lam, and J. H. Siewerdsen. Relative dosimetry using active matrix flat-panel imager (amfpi) technology. *Med Phys.*, (26), May 1999.

[25] J.M. Morand, D.A. Roberts, T.S. Nurushev, L.E. Antonuk, Y. El-Mohri, and B.A. Fraass. An active matrix flat panel dosimeter (amfpd) for in-phantom dosimetric measurements. *Med Phys*, (2), December 2005.

[26] P. A. Jursinic and B. E. Nelms. A 2-d diode array and analysis software for verification of intensity modulated radiation therapy delivery. *Med Phys*, (5), January 2003.

[27] D. Letourneau, M. Gulam, D. Yan, M. Oldham, and J. W. Wong. Evaluation of a 2d diode array for imrt quality assurance. *Radiotherapy Oncology*, (2), February 2004.

[28] T. Wiezorek, N. Banz, M. Schwedas, M. Scheithauer, H. Salz, D. Georg, and T. G. Wendt. Dosimetric quality assurance for intensity-modulated radiotherapy feasibility study for a filmless approach. *Strahlenther Onko*, (7), July 2005.

[29] D. Menichelli, M. Bruzzi, M. Bucciolini, C. Talamonti, M. Casati, L. Marrazzo, M. Tesi, C. Piemonte, A. Pozza, N. Zorzi, M. Brianzi, and A. De Sio. Design and development of a silicon segmented detector for 2d dose measurements in radiotherapy. *Nuclear Instruments and Methods in Physics Research.*, (1), December 2007.

[30] C. Talamontia, M. Bruzzi, M. Bucciolinia, and D. Menichellia. Preliminary dosimetric characterization of a silicon segmented detector for 2d dose verifications in radiotherapy. *Nuclear Instruments and Methods in Physics Research*, (1), December 2007.

[31] S. Amerio, A. Boriano, F. Bourhaleb, R. Cirio, M. Donetti, A. Fidanzio, E. Garelli, S. Giordanengo, E. Madon, F. Marchetto, U. Nastasi, C. Peroni, A. Piermattei, C.J. Sanz Freire, A. Sardo, and E. Trevisiol. Dosimetric characterization of a large area pixel-segmented ionization chamber. *Med Phys.*, (2), November 2004.

[32] Iba Dosimetry. http://www.iba-dosimetry.com/complete-solutions/radiotherapy/imrt-igrt-rotational-qa/matrixxes. website, Jul 2010. Website.

[33] B. Poppe, A. Blechschmnidt, A. Djouguela, R. Kollhoff, A. Rubach, K.C. Willborn, and D. Harder. Two-dimensional ionization chamber arrays for imrt plan verification. *Med Phys.*, (4), February 2006.

[34] S. F. Kry, R. M. Howell, U. Titt, M. Salehpour, R. Mohan, and O. N. Vassiliev. Energy spectra, sources, and shielding considerations for neutrons generated by a flattening filter-free clinac. *Med Phys.*, (5), March 2008.

[35] S.F. Kry, M. Salehpour, D.S. Followill, M. Stovall, D.A. Kuban, R.A. White, and I.I. Rosen. The calculated risk of fatal malignancies from intensity modulated radiation therapy. *I.J. Radiation Oncology*, (4), April 2005.

[36] R.M. Howell, S.F. Fry, E. Burgett, N.E. Hertel, and D.S. Followill. Secondary neutron spectra from modern varian, siemens, and elekta linacs with multileaf collimators. *Med Phys.*, (9), September 2009.

[37] Michael Moll. *Radiation Damage in Silicon Particle Detectors*. PhD thesis, University of Hamburg, 1999.

[38] S. Sze and K. Kwok. *Physics of Semiconductor Devices*. John Wiley & Sons Inc, Hoboken, New Jersey, United States of America, 2007.

[39] Glenn F. Knoll. *Radiation Detection and Measurment*. John Wiley & Sons, Inc, Ann Arbor, Michigan, 2000.

[40] R.C. McGarry, L. Papiez, M. Williams, T. Whitford, and R.D. Timmerman. Leakage current behavior in common i-layer a-si:h p-i-n photodiode arrays. *Mat. Res. Soc. Symp. Proc.*, (21), April 2003.

[41] V. Mishra, V.D. Srivastava, and S.K. Kataria. Role of guard rings in improving the performance of silicon detectors. *Pramana journal of physics*, (2), April 2005.

[42] Australian Nuclear Science and Technology Organisation. http://www.ansto.gov.au/nuclearfacts/benefitsofnuclearscience/irradiationservices/index.htm. website, Jul 2009.

[43] E. Grussell and G. Rikner. Linearity with dose rate of low resisitvity p-type silicon semiconductors. *Phys. Med. Biol.*, (6), June 1993.

[44] M. Petasecca, F. Moscatelli, D. Passeri, G. Pignatel, and C. Scarpello. Numerical simulation of radiation damage effects in p-type silicon detectors. *Nuclear Instrument and Methods in Physics Research Section A: Accelerators, Spectrometers, Detectors and Associated Equipment.*, (1), July 2006.

[45] Academy of Sciences of the Czech Republic-Nuclear Spectroscopy Department. linear accelerator schematic. webpage, Dec 2005.

[46] AAPM. Report 72. Technical report, American Association of Physicists in Medicine, 2001.

[47] G. Rikner and E. Grusell. General specifications for silicon semiconductors for use in radiation dosimetry. *Phys Med Biol*, (9), September 1987.

[48] T Kron & P Hoban P Metcalfe. *The Physics of Radiotherapy, X-rays and Electrons*. Medical Physics Publishing, Madison, Wisconsin, 2007.

[49] S.F. Kry, R.M.Howell, M. Salehpour, and D.S. Followill. Neutron spectra and dose equivalents calculated in tissue for high energy radiation therapy. *Med. Phys*, (4), April 2009.

[50] RD50 Collaboration. Radiation-hard semiconductors for superlhc. In Elsevier, editor, *Physics Research Section A: Accelerators, Spectrometers, Detectors and Associated Equipment*, volume 541 of *12*, pages 189–201. Elsevier, Apr 2005.

[51] K. Nagai, T. Sekigawa, and Y. Hayashi. Capacitance-voltage characteristics of semiconductor-insulator-semiconductor (sis) structure. *Solid State Electronics*, (8), July 1985.

[52] G. Lindstrom, M. moll, and E. Fretwurst. Radiation hardness of silicon detectors- a challenge from high-energy physics. *Nuclear Instrument and Methods in Physics Research Section*, (1), April 1999.